Università degli Studi di Napoli
Federico II

Facoltà di Scienze Matematiche, Fisiche e Naturali

Dottorato di Ricerca in Scienze Chimiche

XVIII Ciclo

PhD Report

Application of Computational Models to the Study of Molecular Sensors

Dottorando:

Dott. Gaetano Festa

Tutore:

Prof. Maurizio Cossi

Coordinatrice:

Prof.ssa Rosa Lanzetta

AA 2004-2005

Introduction

Computer simulation started as a tool to exploit the electronic computing machines that had been developed during and after the Second World War. These machines had been built to perform the very heavy computation involved in the development of nuclear weapons and code breaking. In the early 1950s, electronic computers became partly available for nonmilitary use and this was the beginning of the discipline of computer simulation.

The strange thing about computer simulation is that it is also a discovery, albeit a delayed discovery that grew slowly after the introduction of the technique. In fact, discovery is probably not the right word, because it does not refer to a new insight into the working of the natural world but into a new approach to the study of natural phenomena[1].

Computing in the natural sciences and engineering has gained considerably in importance as a result of the ever increasing power of available hardware. As a consequence it is justified to speak of the tripod of science: experiment, theory and computing. The first two of these branches should not require an explanation. The third, computing, comprises ”computer experiments” which give exact results - up to rounding errors and errors in computer programs - within a model ultimately defined by the computational procedures applied, i.e. by the assumptions on which they are based. The better the model and the justification for assumptions, the better and the more real-

istic the results. Scientific computing thus permits the prediction and checking of results of experiments and especially their interpretation. This clearly will never make experiments superfluous - but it will change and has already changed the way in which experiments are designed and selected. It have to be just reminded the importance of computer modelling in the design of air planes, jet engines, cars, and computers, in oil exploration and weather forecasting, to name just a few fields essentially shaped by modern simulation techniques.

The central problem is here the approximate but sufficiently accurate solution of the molecular Schrödinger equation. This is a formidable task simply because of the dimensionality: the wavefunction describing a system of electrons and nuclei is a function of cartesian coordinates (all problems mentioned above are three-dimensional cases), which is simply not manageable in an accurate way. Despite these apparently insurmountable difficulties, chemists now almost routinely perform calculations for systems with a few hundred atoms, which give results that are competitive in accuracy and effort with measurements[2].

Already in the 70's and 80's, quantum chemical methods were very successful in describing the structure and properties of organic and main-group inorganic molecules. The Hartree-Fock (HF)[3] method and its simplified semi-empirical modifications became standard tools for a vivid rationalization of chemical processes. The underlying molecular orbital (MO) picture

was, and still is, the most important theoretical concept for the interpretation of reactivity and molecular properties. Nevertheless, quantum chemical methods were not used extensively for industrial problems, although most of the industrial chemistry produces organic compounds. One reason can be found in the fact that almost all industrial processes are catalytic. The catalysts are predominantly transition metal compounds, which in general have a more complicated electronic structure than main-group compounds, since their variability in the occupation of the *d* orbitals results in a subtle balance of several close lying energy levels. HF and post-HF methods based on a single electron configuration are not able to describe this situation correctly. Furthermore, the catalyst systems were generally too big to be handled so as to impose the use of small model systems. Such investigations provided only a basic understanding of the catalytic reaction, but no detailed knowledge on steric and electronic dependencies. With the improvement of both the methodology and the algorithms of density functional theory (DFT) in the last two decades, the situation changed significantly. DFT appears to be less sensitive to near degeneracy of electronic states, and furthermore incorporates some effects of electron correlation. The development of new functionals with improved description of non-uniform electron distributions in molecules or on surfaces, paved the way for a qualitative or even quantitative quantum chemical treatment of a large variety of transition metal compounds and their reactions. Although the chemical processes in many cases involve transition

metal compounds, calculations on pure organic molecules are still important to predict properties like thermodynamic data or various types of spectra[4].

It is now well established that molecular calculations with atom centered functions can be carried out in computational times that scale linearly with system size in the large system limit. This has been achieved through the use of Gaussian orbitals in Kohn-Sham DFT calculations[5], fast multipole methods for the Coulomb problem, and density matrix search alternatives with sparse matrix multiplication techniques to bypass the $O(N^3)$ Hamiltonian diagonalization bottleneck.[6]

Nowaday, the industrial scenario is changing and the recourse to such tools appear more often in industries. This is particularly true in the field of drug design and nanotechnologies, in which the use of simulation is fundamental. From the economical point of view this methods take many advantages with respect to classical purely experimental practices. This is due not only on innovation grounds for competition purpouses but for economical saving question. Infact, expecially in nanotechnology, the various materials required are very expensive because they are very innovative and it can not be possible to take advantage of series productions, so direct trial and error experimentation proceedings are economically prohibitive.

Instead, simulation require an initial investment in computer resources that will be widely refund during production. Moreover, nowaday it is possible to use services offered by specialized computing centers or GRID new emerging

technologies that require just a computer connected to Internet. So, it is very promising the use of this methodologies as an effective tool that can be added to the arsenal available to the chemists whatever will be their specific field of application.

Contents

Part I

Ab initio Molecular Dynamics IR Spectra Simulation

Chapter 1

IR Spectra Simulation of Uracil

Infrared radiation is absorbed and converted by molecules into energy of molecular vibration. This absorption is quantized, but vibrational spectra appear as bands rather than lines because a single vibrational energy change is accompanied by a number of rotational energy changes. The frequency of absorption depends on the relative masses of the atoms, the force constants of the bonds, and the geometry of the atoms, that is, its chemical environment.

There are fundamentally two types of molecular vibrations: stretching and bending. A stretching vibration is an oscillating movement along the bond axis such that the atomic distance changes. A bending vibration instead is related to more complex motions that can go from a simple bond angle oscillation involving just three connected atoms to a more complex composit

motion in which many atoms can be involved, e.g., twisting, rocking, and torsional vibration. Only those vibrations that result in an oscillating change in dipole moment of the molecule are observed in infrared spectra. The alternating electric field, produced by the change in charge distribution accompanying a vibration, is coupled with the oscillating electric field of the electromagnetic radiation causing the transfer of energy.

In practice, functional groups that have a strong dipole give rise to strong absorption in the infrared. To complicate further this scenario one have to consider the possibility of coupling when vibrations share a common atom. Moreover, it has to be considered also hydrogen bonding and Fermi resonance arising from the combination of fundamental vibrations and overtones[7].
Full interpretation of infrared spectra is a formidable task and it is not always possible to resolve it easily by the application of simple empirical rules so theoretical calculations are fundamental tools in achieving this target. From this point of view, in the context of present work, it is possible to trace fundamentally two routes to calculate frequencies: *ab initio* molecular dynamics (MD) and analytical energy derivatives techniques.

Classical molecular dynamics using predefined potentials, either based on empirical data or on independent electronic structure calculations, is well established as a powerful tool to investigate many bodies condensed matter systems. At the very heart of any molecular dynamics scheme is the question of how to describe the interatomic interactions. The traditional route followed in

molecular dynamics is to determine these potentials in advance. Typically, the full interaction is broken up into two bodies, three bodies and many bodies contributions, long range and short range terms, etc., which have to be represented by suitable functional forms. After decades of intense research, very elaborate interaction models including the nontrivial aspect to represent them analytically were devised. Despite overwhelming success the need to devise a fixed model potential implies serious drawback. Among the most delicate ones are systems where many different atom or molecule types give rise to a myriad of different interatomic interactions that have to be parameterized and the electronic structure, and thus the bonding pattern, change qualitatively in the course of the simulation[8].

The basic idea underlying every *ab initio* molecular dynamics method is to compute the forces acting on the nuclei from electronic structure calculations that are performed ”on the fly” as the molecular dynamics trajectory is generated. In this way, the electronic variables are not integrated out beforehand, but are considered as active degrees of freedom. This implies that, given a suitable approximate solution of the many electron problem, also chemically complex systems can be handled by molecular dynamics. But this also implies that the approximation is shifted from the level of selecting the model potential to the level of selecting a particular approximation for solving the Schrodinger equation. Applications of *ab initio* molecular dynamics are particularly widespread in materials science and chemistry, where the aforemen-

tioned difficulties are particularly severe.

The Car-Parrinello (CP) [9] method has become a central tool in *ab initio* molecular dynamics simulations over the last several years. The CP method is essentially an extended Lagrangian[10] MD scheme in which the electronic degrees of freedom are not iterated to convergence at each step, but are instead treated as fictitious dynamical variables and propagated along with the nuclear degrees of freedom by a simple adjustment of time scales. The resultant energy surface remains close to a converged adiabatic electronic surface. Such an approach offers significant computational advantages for efficient MD calculations. In the original CP approach, the Kohn-Sham molecular orbitals ψ_i were chosen as dynamical variables to represent the electronic degrees of freedom. However, this is not the only possible choice, and alternative approaches are proposed in which the individual elements of the reduced one-particle density matrix, P, are explicitly treated as dynamical variables. Car-Parrinello calculations are usually carried out in a plane wave basis set. These form an orthonormal basis that is independent of the atom positions. Although most of the integrals can be calculated easily using fast Fourier transform methods, a very large basis set is needed to represent the orbitals to the desired accuracy. The problem is less severe if pseudopotentials are used to replace the core electrons, since the plane wave basis does not easily describe the cusps and high electron density near the nuclei. Recently, Gaussian orbitals have also become a useful adjunct to treat this problem. Compared to a plane wave ba-

sis, far fewer Gaussians are needed to achieve a desired accuracy, since they are localized in regions of higher electron density and follow the nuclei as they move. The necessary integrals are somewhat more difficult to calculate than for a plane wave basis, but very efficient algorithms are available to calculate these integrals and their derivatives with respect to the atom positions.

In an orthonormal basis, an extended Lagrangian for the system can be written as

$$L = \frac{1}{2}Tr(V^T MV + \frac{1}{2}\mu Tr(WW) - E(R,P) - Tr[\Lambda(PP-P)] \qquad (1.0.1)$$

where M, R, and V are the nuclear masses, positions, and velocities, respectively. The density matrix, density matrix velocity, and the fictitious mass for the electronic degrees of freedom are P, W, and μ, respectively. Constraints on the total number of electrons, N_e ,and on the idempotency of the density matrix are imposed using a Lagrangian multiplier matrix Λ. The energy is calculated as

$$E = Tr[hP + \frac{1}{2}G(P)P] + V_{NN}, \qquad (1.0.2)$$

where h and $G(P)$ are the one and two electron matrices and V_{NN} is the nuclear repulsion energy. Using the principle of stationary action[10] for the Lagrangian in 1.0.1 , the Euler-Lagrange equation for the propagation of the density and the nuclei can be set up and solved properly to obtain the trajectory[6].

In the framework of *ab initio* molecular dynamics a given property of the

system will be calculated as a Fourier Transform of proper auto-correlation function[11] derived by the sampling of trajectories. In the case we are interest in, that is IR spectra, the proper function is the dipole autocorrelation function built sampling the *ab initio* Density Matrix Propagation (ADMP) Molecular Dynamics trajectoy as:

$$C(t) =< \mu(0)\mu(t) >= \sum_t \mu_0\mu_t \tag{1.0.3}$$

where μ_t is the dipole moment at a given time t (t=0 beginning of simulation). At this point phylosophical questions arise about the meaning itself of dipole moment, μ, because this is a macroscopic property of the system connected to the electric response of the whole system. Many authors have given different definitions to this property and consequently there are different theories to describe such a quantity. Due to the extreme complexity of real systems, as usual in science, a reductionistic approach is needed and in this work, the dipole moment of the system has been represented as the dipole moment of a single molecule.

The dipole auto-correlation function Fourier Transform allows to pass from the time variables to the frequency domain, obtaining the spectrum

$$\alpha(\omega) = \int_{-\infty}^{\infty} e^{-i\omega t} < \mu(0)\mu(t) > dt \tag{1.0.4}$$

Moreover, in this formalism it is possible to take advantage of the fact that the spectra can be resolved unambiguously comparing the Fourier Transform of the bond, angle, or whatever vibrational motion autocorrelation functions

directly with the simulated IR spectra. For example, in the case of a stretching motion the corresponding autocorrelation function, $S_i(t)$, will be defined as

$$S_i(t) = < R_i(0) R_i(t) > \tag{1.0.5}$$

where $R_i(t)$ represent the bond length i at time t. So, $\Sigma_i(\omega)$, defined as

$$\Sigma_i(\omega) = \int_{-\infty}^{\infty} e^{-i\omega t} S_i(t) dt \tag{1.0.6}$$

will be a signal with a direct correspondence in the simulated IR spectra. This property is due to the fact that dipole moment oscillations follow exactly the oscillations in the structural parameters that generate it. The only difference in this context is that dipole moment function is the resultant of the superposition of each active oscillating motions.

Furthermore, theoretical computations of vibrational frequencies for polyatomic molecules have become in the last years unvaluable aids to spectroscopists thanks to the increasing availability of computer codes allowing the analytic evaluation of first and second energy derivatives, and to the increased power of affordable computers.

The quantum chemistry and statistical mechanics of molecular systems are two branches of theoretical chemistry that are of vital importance in physical chemistry. Methodology and computational demands of these two disciplines are, in practice , rather different. As a result, they are usually separated by an intermediate modeling step transforming the results of the electronic structure

calculation in parametrized model potentials. In the *ab initio* molecular dynamics method, the nuclear gradients obtained from a continuously updated electronic structure computation are directly applied as mechanical forces. Construction and parametrization of models is avoided. Electronic structure calculation and finite temperature statistical mechanics are unified at a fundamental level in *ab initio* MD. First-principle rigor, of course, comes at a considerable computational cost, limiting the size of model systems and the time span over which they can be followed. The methodologies taken in account here differ in the fact that the ADMP introduce an exact electronic potential, treating the motion according to Classical Mechanics, while in the harmonic and anharmonic models the potential is approximated by a series expansion, but the motion is treated quantum mechanically.

Applications in physical chemistry for which the extra expense of direct dynamics has paid off typically involve ionic or polar liquids characterized by strong coupling between electronic structure and thermal fluctuations. A prominent example is the chemistry of aqueous ionic solutions. Classical reactions such as acid-base and redox equilibria of simple ions fall in this category but also a large fraction of the complex reactions of biochemistry.
Later on we will be interested in nucleic acids that can be exposed to water solvent in a number of biological structures. The hydration of nucleic acids is therefore of great interest and has been investigated extensively by infrared spectroscopy. Because of their role as building blocks, also single bases sol-

vated in water have been the subject of spectroscopic study. These relatively small aqueous molecules are very suitable targets for *ab initio* molecular dynamics simulation methods, and therefore, we chose the computation of the infrared spectrum of uracil[12], the smallest of nucleic bases, to illustrate the potential of ”first-principle” vibrational spectroscopy as a new tool in the computational chemistry of complex molecular systems.

1.1 Computational Details

To generate the reference geometry and electron density for the MD simulation we used Gaussian 03 package and it has been done at the B3LYP/6-31+G(d,p) level. For the integration of the equations of motion the velocity-Verlet algorithm [1] was used.

A total integration time of 10 ps was used so as to ensure a proper repre-

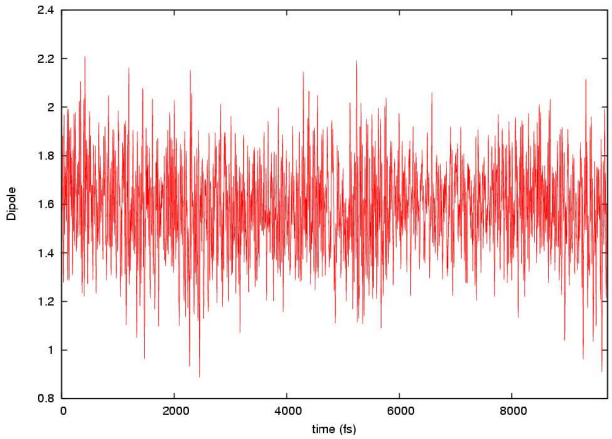

Figure 1.1: Sampled dipole moment function.

sentation of vibrational motions. According to Nyquist guidelines about the

[1] This algorithm is based simply on truncated Taylor series expantion of the particle coordinates r as:

$$r(t+\Delta t) = r(t) + v(t)\Delta t + \frac{f(t)}{2m}\Delta t^2 + ...$$

where r(t) are the coordinates at time t, while f(t) are the forces. After proper rearrangement it is possible to obtain successively the coordinates at future time[1].

proper sampling of periodic functions, a time step of 0.2 fs ensure no lost of information in sampling the oscillating dipole moment function[13]. The importance of a proper choise of time step is also fundamental to preserve the theoretical validity of the solution of the equations of motion due to round-off error[1]. The function so obtained is shown in figure 1.1. A 128 a.u. fictitious mass of electron has been chosen ensuring a good separation between the electronic and nuclear degrees of freedom. Conservation of total energy is shown in figure 1.2 and it is conserved within 0.004 Hartree.

The analytical frequencies calculation needed as test reference have been

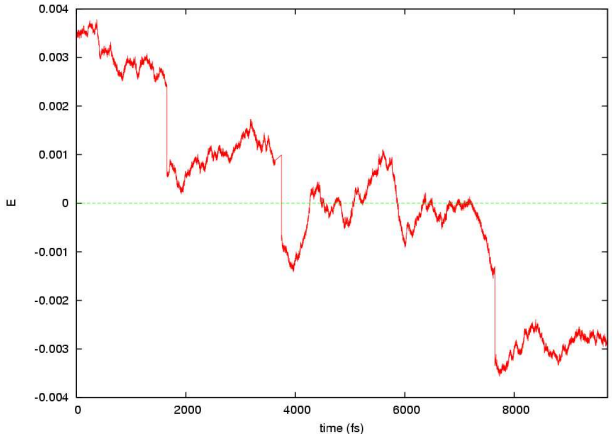

Figure 1.2: Change in total energy during the simulation.

performed with a locally modified version of the Gaussian 03 package[14] using the B3LYP functional and the 6-31G(d) basis set adding diffuse and polarization functions optimized for correlation methods, togheter with filed-induced polarization functions.

Details about the implementation of anharmonic computation are given elsewhere [15, 16].

1.2 Results

Trajectory was started at the uracil equilibrium geometry obtained using DFT theory[5] with B3LYP[17] hybrid exchange-correlation functional and all electron Pople basis set 6-31+G(d,p) with polarization and diffuse functions, giving a planar structure (C_s symmetry, Figure 1.3). In table 1.1 are reported the

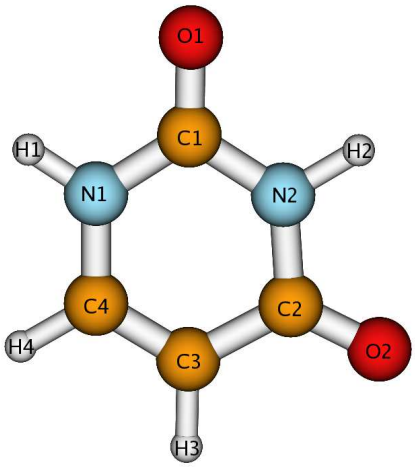

Figure 1.3: Geometry of uracile at B3LYP/6-31+G(d,p) level.

corresponding geometrical parameters. This data are compared with experi-

mental estimates obtained from electron diffraction[12] and show a satisfactory agreement. In order to have a more quantitative estimation of the errors they have been calculated as:

$$err = \frac{\sqrt{\sum_{i=1}^{N}(x_i - x_i^{Exp})^2}}{N} \tag{1.2.1}$$

where the x_i's will be substituted with the bond lengths and angles, for which it has been found, respectively, a mean error of 0.004 Å and 0.82°. So we can consider this geometry as a satisfactory starting point for the simulation. Here, as a preliminary work, it has been considered just the dipole moment of the single molecule without any interaction with the neighbourhood.

Table 1.1: Equilibrium geometrical parameter of Uracil at B3LYP/6-31+G(d,p) level.

bond length (Å)			bond angle (°)		
bond	computed	exp[a]	angle	computed	exp[a]
C(1)-N(1)	1.396	1.399	C(1)-N(1)-C(4)	123.7	123.2
C(1)-N(2)	1.385	1.399	C(1)-N(1)-H(1)	114.9	115.1
C(1)-O(1)	1.217	1.212	C(1)-N(2)-C(2)	128.4	126.0
C(2)-O(2)	1.219	1.212	C(1)-N(2)-H(2)	115.5	129.3
C(2)-N(2)	1.414	1.399	C(2)-C(3)-C(4)	120.0	119.7
C(2)-C(3)	1.460	1.462	C(2)-N(2)-H(2)	116.1	116.1
C(3)-C(4)	1.350	1.343	C(3)-C(2)-N(2)	113.3	115.5
C(3)-H(3)	1.081	1.072	C(3)-C(2)-O(2)	126.3	124.3
C(4)-H(4)	1.085	1.072	C(4)-N(1)-H(1)	121.4	121.0
N(1)-H(1)	1.011	1.002	C(4)-C(3)-H(3)	122.0	122.5
N(2)-H(2)	1.014	1.042	N(1)-C(4)-C(3)	122.0	122.1
N(1)-C(4)	1.376	1.399	N(1)-C(1)-N(2)	112.7	114.0
			N(1)-C(1)-O(1)	122.8	123.7
			N(2)-C(1)-O(1)	124.5	121.9
			O(2)-C(2)-N(2)	120.4	120.2
			H(3)-C(3)-C(2)	118.1	118.9
			H(1)-N(1)-C(1)	115.5	115.1
			H(4)-C(4)-C(3)	122.9	122.8

[a]Experimental value X-ray from ref. [12]

In figure 1.4 is drawn the dipole moment autocorrelation function obtained sampling the 10 ps trajectory according to equation 1.0.3. Clearly this is an

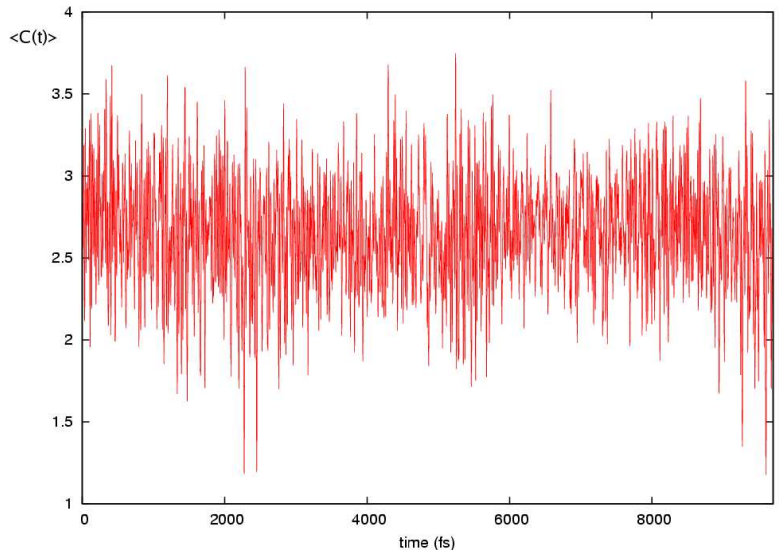

Figure 1.4: Dipole autocorrelation function based on uracile trajectory of 10 ps.

oscillating function reflecting the fact that the dipole moment of the molecule itself oscillates around its equilibrium value, as expected for this type of properties.

In figure 1.5 we report the spectra obtained according to the ADMP method explained at page 6. In order to check the reliability of this method as an effective tool in computational chemistry the spectra have been compared with both experimental data and more sophisticated computational methods.

As experimental reference has been chosen the IR spectra of uracil at low

temperature in argon matrix[18]. This is a good approximation to the purely vibrational spectra of isolated species. In such experimental conditions the interactions between the environment and the studied molecule are minimized. Below, are reported the same spectra simulated by analytical frequencies calculation in the framework of Quantum Mechanics. In figure 1.6 are sketched this spectra. Band width are represented arbitrarily as Lorentzian function with 0.5 cm^{-1} half-width. Infact, in this calculations it is not possible to have an estimate of the band width but only band positions and intensity can be estimated.

In table 1.2 are reported the frequencies taken from the IR spectra in argon

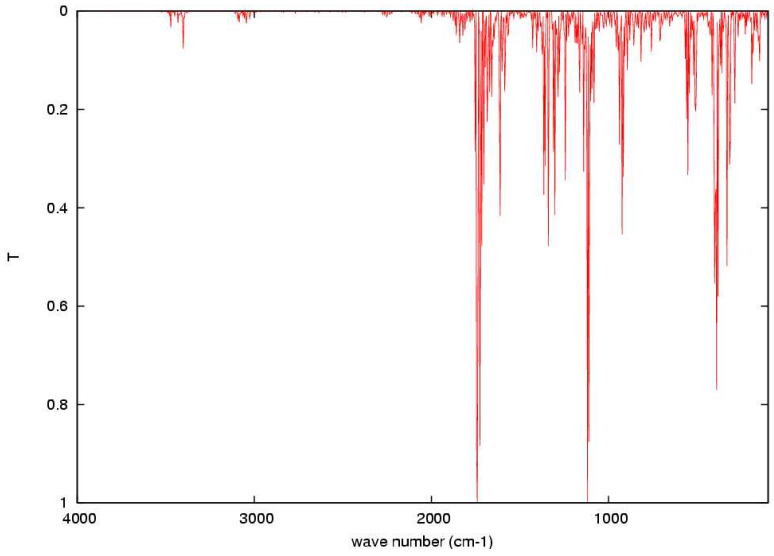

Figure 1.5: Spectra of Uracil obtained by ADMP trajectory.

matrix and calculated with the above mentioned methods. That is, by ADMP simulation and within both harmonic and anharmonic approximations. The mean error with respect to experimental data, according to equation 1.2.1, were found to be: 125 cm^{-1} for the ADMP spectra; 277 and 97 cm^{-1} for the harmonic and anharmonic approximations, respectively. The discrepacies among the ADMP simulated spectrum and the analytical frequency calculations are 33 and 17 cm^{-1}, for the harmonic and anharmonic model, respectively. The ADMP simulated spectrum represent a good approximation having given results situated intermediately between the harmonic and anharmonic spectra, suggesting improvements with respect to the harmonic model.

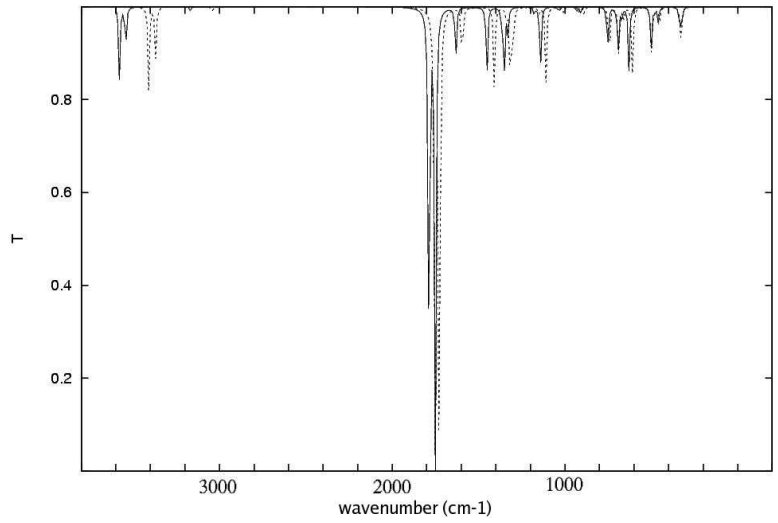

Figure 1.6: Spectra of Uracil simulated, harmonic and anharmonic.

Below the identification of some bands in the simulated spectra is reported, with deviation from the experimental values in parenthesis, all frequencies being in cm^{-1}.

In uracil two carbonyl groups are attached to the etherocyclic ring and the vibrations of these groups may be coupled together. The typical pattern of the transmission bands due to the carbonyl stretching vibrations of uracil and its derivatives is always very complex. It is commonly believed that the Fermi resonance of fundamentals with combination bands is responsible for this complexity in the experimental spectra.

In the present case the higher frequency mode can be better described as an in-phase stretching and the lower frequency mode as an out-of-phase stretching located, respectively, at 1746(-18) and 1720(1) cm^{-1}.

The bending in-plane vibrations of carbonyl groups can be better described as in-phase rocking and out-of-phase scissoring movements. This contribute to two frequencies at 568(9) and 542(6) cm^{-1} for rocking while the scissoring take part in the mode with frequency 389(-2) cm^{-1}.

Similar spectra position of the bands due to carbonyl rocking and scissoring were also observed in the matrix spectra of substituted uracil. This band positions are shifted up and down with respect to the position of the single band observed in analogous compounds with only one carbonyl group. This shift is due to the relatively strong coupling between the two carbonyl bending vibrations.

Table 1.2: Comparision of experimental IR spectra in Ar matrix with calculated data obtained both with ADMP simulation and with analytical frequencies calculations.

exp[a]	ADMP	harmonic[b]	anharmonic[b]
3485	3472	3640	3470
3435	3402	3603	3429
	3086	3269	3127
	3043	3229	3102
1764	1746	1847	1812
1719	1720	1810	1787
1644	1610	1692	1655
1472	1427	1512	1469
1399	1405	1430	1400
1389	1365	1413	1376
1359	1339	1390	1358
1217	1238	1238	1213
1185	1120	1202	1170
1069	1081	1095	1072
987	958	992	979
982	936	969	949
958	923	968	947
804	818	813	804
759	765	773	751
757	752	752	747
717	704	730	719
662	656	689	668
559	568	558	549
550	551	561	560
536	542	541	533
516	511	519	513
393	405	395	392
391	389	385	385
	192	170	168
	148	149	149

[a] Experimental IR Spectra in Ar matrix from ref. [18]

[b] Analytical frequencies calculation at B3LYP/6-31+G(d,p) level

The out-of-plane carbonyl bending vibrations are positioned at 752(-5) cm^{-1} due to C(1)-O(1) vibration, while C(2)-O(2) contribute mainly to the signal at 818(14) and 704(-17) cm^{-1}.

The bands due to the N(1)-H and N(2)-H bond stretching are observed, respectively, at 3472(-13) and 3402(-33) cm^{-1}. Analogously, the frequencies in which the main contribution comes from in-plane bending vibrations are at 1427(-45) and 1405(6) cm^{-1}, while the out-of-plane NH bending vibrations are positioned at 551(1) and 656(-6) cm^{-1}.

The intensity pattern is different and further investigations are required to bring to light such differencies, in particular, some insights could be found considering that for the ADMP simulation a more sofisticated statistical treatment is required considering the simulation in cells of a properly chosen statistical ensemble, so as to introduce quantum correction with a properly desymmetrization factor derivied from the requirement to satisfy the detailed balance[19]. This discrepacy could also be attenuated increasing the size of the electronic basis set, such as adding more diffuse and polarization function, so as to improve the description of polarizability of the system, or increasing the time integration path. Infact, in test simulations were observed a change in the intensity pattern consequently to the increase of time integration path.

1.3 Conclusions

Current work was focused on the study of a new methodological approach to obtain spectroscopical properties. The present method, based on the auto-correlation function formalism sampling ADMP trajectory has shown satisfactory agreement not only with analytical energy derivatives methodologies, but more important with experimental data obtained in experimental conditions so as to reproduce chemical situations comparable to that of simulation. That is, attenuation of interaction with environment due to the acquisition of spectra in argon matrix.

In particular, the mean error was 125 cm^{-1} with respect to experimental data, while a mean error of 33 and 17 cm^{-1} with respect to harmonic and anharmonic models, respectively. This results showed a clear improvement of ADMP spectrum with respect to the harmonic approximation. In the context of MD simulation this can be considered as a preliminary work that requires further refinements so as to include solvent effects. For the inclusion of solvent effects it is possible to follow the route of Polarizable Continuum Model (PCM)[20] or an explicit treatment of solvent molecules. In the former case, the solvent should be treated as a perturbation in the Hamiltonian of the molecule. In the latter case, this could be achieved treating the solvent molecules at the same level of theory used for the solute description or with techniques that allow a differential treatment of different parts of the system,

such as ONIOM or other hybrid QM/MM methods.

In any case, it should not be excluded that both techniques could be used simultaneously, treating the first shell of solvation explicitly and the remaining solvent within PCM framework.

In conclusion, even though the results obtained here are in fair agreement with the compared data, further studies are required so as to extend the application of this methods to the spectroscopic study of such a system in biological environment.

Part II

Silicon Surface Based Sensing

Since the invention of the transistor in 1947, there has been a widespread and continuing interest in understanding the physical and chemical properties of semiconductor surfaces. Despite the fact that the first transistor was made from germanium, over the last years, silicon has completely substituted it. This is due in part to the presence of robust native oxide on silicon surfaces that protects it from further oxidation, but also to its greater abudancy respect to germanium[2], currently used mainly for wireless applications[21].
Microelectronics remains one of the few areas of technology where it is essential to use single crystals of well-defined crystallographic orientation. Many of the rapid advances in microelectronics over the last years, particularly since the advent of the personal computer, have been attained through a reduction in size leading to the well known Moore's Law according to which computing power doubles every sixteen months. Common microprocessors now use 0.35 μ m technology. Continuing trends in microelectronics over the next 10-15 years will likely also require the ability to understand and control the surface chemistry of silicon and other semiconductors on length scales of less than 100 $\AA$ dimensions[22].

This interest is not only for the many technological applications presently in use and envisioned for the future, but also from a fundamental perspective. Infact, much remains to be understood about the surface reactivity of

[2]Infact, silicon is the most abundant element on the earth surface after the oxygen with which is usually bounded.

these materials, despite their ubiquitous presence in microelectronics. From a technological standpoint the already mentioned native oxide coverage represents also a problem and requires an alternative coverage so as to prevent such oxidation and at the same time giving interesting electric properties to the material. Formation of Si-C bonds on surface have shown to have the right behavior. So, at the heart of this new technology is the ability to understand how chemical reactions can occur on the surface, acquiring as much as possible control on the processes involved. While the reactivity on a surface often parallels that of the solution-phase molecular silanes, there are many cases where perturbations or electronic effects from the underlying bulk can have dramatic consequences on the reaction pathway and outcome. In other situations, the electroactive behavior of the semiconductors can be utilized to drive surface chemistry, thus permitting access to reactions that are unknown in molecular systems. This incredible diversity is just now coming to light[23].

The surface of silicon have several different chemical handlers through which functionalization may be carried out. It is possible to trace out fundamentally two routes to such functionalizations: wet chemistry and Ultra High Vacuum (UHV) chemistry.

Wet chemical reactions require a metastable surface to successfully carry out surface chemistry. The precursor surface must be stable enough to handle at atmospheric pressure in the presence of solvent vapors, inert gas impurities,

and other contaminants and still reactive enough to undergo chemistry. Both (100) and (111) surfaces that are known to have this bipolar character are Si-H and Si-X (X= Cl, Br, I) terminated silicon. The Si-H terminated surface is relatively stable in air for short periods; in contrast, the Si-X derivatized surface is much more reactive with respect to hydrolysis and Si-OH formation and can generally only be handled under inert atmosphere. The hydride-terminated surfaces in general offer many advantages, including their excellent chemical homogeneity ($>$ 99% H termination) and strong FTIR stretching modes (2100 cm^{-1}) which can provide information as to surface flatness and makeup.

Wet chemical approaches will start with a reaction motif known for decades in the molecular organosilicon literature as hydrosilylation, and then diverge into electrochemical and other routes toward Si-C bonds on surfaces. Hydrosilylation involves insertion of an unsaturated bond into a silicon-hydride group. Alkyne and alkene hydrosilylation on Si-H-terminated surfaces yield alkenyl and alkyl termination, respectively. A radical mechanism was proposed for monolayer formation under these conditions. The initiator undergoes homolytic cleavage to form two radicals which decompose to an alkyl radical. The alkyl radical can then abstract H from a surface Si-H group to produce a silicon radical. Because silyl radicals are known to react extremely rapidly with olefins, formation of a silicon carbon bond is the next probable step. The carbon-based radical can then abstract a hydrogen atom either from a neighboring Si-H group or from the allylic position of an unre-

acted olefin. It was observed that this reaction could occur in the absence of radical initiator at higher temperatures ($\geq$ 150 °C), almost certainly through homolytic Si-H cleavage, $Si-H \rightarrow Si\cdot + H\cdot$. This yields the silicon surface-based radical (dangling bond) which can then react via the previous mechanism. Aliphatic monolayers produced on hydride-terminated Si(111) and Si(100) through the thermal hydrosilylation of alkenes are stable up to 600 K under vacuum, which indicates that organic monolayers on silicon can be thermally resistant. A major limitation of this appoach is the large excess of alkene required. It is known that hydrosilylation of unsaturated compounds can also be promoted by UV irradiation due to homolytic cleavage of Si-H bonds, as is the case with thermal induction. UV photoinduction, however, takes place at room temperature and thus provides a way to avoid thermal input that could be harmful to delicate or small features on a silicon chip. In contrast to flat, hydride-terminated silicon surfaces, a simple white-light source can induce hydrosilylation of alkenes and unconjugated alkynes on Si-H-terminated photoluminescent porous silicon surfaces at room temperature in minutes. The reaction requires the porous silicon samples to be photoluminescent and is not dependent upon morphology or doping. Because the reaction is photoinduced, photopatterning can be easily carried out with simple optical apparatus to prepare spatially defined areas of differing chemical functionalities as small as 30 μ m. This approach is of interest in that it has no parallels with the chemistry of either bulk silicon surfaces or molecular

silanes. It functions purely as a result of the nanoscale size of the features in porous silicon and is tied intimately with the unique photoluminescence of this material.

Electrochemistry has also been used to produce close-packed organic monolayers on hydride-terminated flat silicon surfaces. This reaction utilizes the electrode nature of the semiconducting silicon, no clear reaction parallels can be found for soluble, molecular silanes. One important advantage of this approach is that the process is cathodic, thus making the surface electron rich during the reaction, which renders it less susceptible to nucleophilic attack by water, suppressing oxidation.

UHV (Ultra High Vacuum) , on the other hand, permits reactivity studies of surfaces much too reactive for even inert atmosphere handling. UHV surface functionalization strategies offer the possibility to study surfaces in conditions that are , as close as experimentally possible, perfect at the atomic level. Operating at pressures below 10^{-10} mmHg, surfaces can be routinely heated to temperatures greater than 1000 K without oxidation, allowing access to unusual (and thermally stable) reconstructions that are otherwise unattainable, even under inert atmosphere. In addition, working under UHV permits exquisite STM imaging of the surface-bonded molecules. Molecular modeling of these interfaces has also been studied in detail because of the high order of the interface. Research on small unsaturated hydrocarbons such as ethylene, propylene, acetylene, and benzene has shown that they chemisorb

to Si(100)-2×1 surfaces at room temperature and that the products are able to resist temperatures of up to $550 \div 600K$. The experimental work of many groups clearly indicates that alkenes add to clean Si(100)-2×1 surfaces to form a formal [2+2] cycloaddition product. Two new Si-C bonds are formed due to cleavage of the bonds in the alkene and disilylene, with the Si-Si bond remaining intact as shown by different experimental techniques. Concomitant rehybridization of the two sp^2 carbons to sp^3 takes place. Theoretical analyses of the [2+2] additions indicate that there is no stable minimum for a structure with a broken Si-Si bond[24]. Acetylene reacts in a similar [2+2] fashion yielding a disilicon-substituted alkene[25]. Computational studies have substantiated the [2+2] addition reaction of alkenes and alkynes to the surface and indicate cleavage of the weak bond, leaving the σ-like bond intact[26].

Concerted [2+2] cycloadditions are normally symmetry-forbidden in molecular systems and hence very slow, suggesting that a low-symmetry pathway may be accessible on the surface. The weakness of the bond may actually suggest more of a diradical character, with an unpaired electron on each silicon atom. The dimers can also tilt on the surface, leading to zwitterionic character, with each silicon atom having a partial positive or negative charge. The actual properties of the silicon dimers may be a combination of these representations. It is clear that a simple σ and π bonding picture of these dimers cannot explain the ease at which [2+2] cycloadditions occur. The tilting of the dimers on the surface, based on calculations, leads to bending of the sili-

con dimer bond axis from a planar arrangement, causing charge polarization of the dimer and making the π^* orbital at one end susceptible to attack by nucleophiles, which leads to a much higher reaction probability. Olefins and alkynes with secondary functional groups, such as a second alkene, nitrogen, or aromatic group, can also undergo the [2+2] reaction, leading to a more highly functionalized surface. A wide range of complex olefins react in this manner at moderate temperatures.

The surfaces prepared through both techniques have proven themselves to be very robust with respect to demanding chemical and oxidative conditions. Further chemistry has been carried out on these interfaces to prepare more sophisticated surfaces for a variety of applications. Sensor design, surface-related assays, spectroscopic handles, and biological molecule interfacing and others were proposed as driving forces for this exciting area of research. Traditional protecting group strategies may be viable options when preparing functional films on silicon.

Many generalizations can now be made about the organometallic surface chemistry of silicon[27]. Still, more questions remain, especially concerning the nature of packing and bonding of organic groups, the bonding and reactivity of the silicon-silicon dimers on the Si(100)-2×1 reconstructed surface, the stability of all these surfaces over the long term, their biocompatability, and many other important questions. This field is in a close proximity between fundamental science and technological applications, and it is only a matter of

time and circumstance before tailored organic interfaces reach their commercial potential.

Chapter 2

Hybridization of Si(100)-2$\times$1 Surface by ACP

Introduction Research on DNA-modified surfaces has become increasingly active in recent years and is expected to have soon a major have a broad-based impact on a number of emerging biotechnology areas, such as DNA chip technologies and DNA computing[28]. An important area in biological monitoring is the sensitive diagnosis of diseases, biological species, or living systems (bacteria, virus or related components) at ultratrace levels in biological samples (e.g. tissues, blood, and other bodily fluids) and environmental samples (e.g. air, soil and water). To detect a compound in realistic sample a biosensor must be able to recognize and discriminate among various biochemical

constituents of these systems in order to provide unambiguous identification and accurate quantification. Living systems possess exquisite recognition elements (e.g. antibody, enzyme, gene probes, etc.), often referred to as bioreceptors, which allow specific identification and detection of complex chemical and biological species. Biosensors are devices that exploit this powerful molecular recognition capability of bioreceptors[29].

Optimization of surface chemistry for surface-based analysis of biomolecules such as DNA requires careful attention to the chemistry of DNA attachment in order to maximize the density of DNA binding sites, while retaining high selectivity against sequences with small numbers of mismatches. Degradation of the interface may occur during the initial attachment chemistry or during the subsequent hybridization and denaturation processes. Many research are focused on identifying the specific chemical and structural factors that lead to robust DNA-functionalized surfaces, to develop attachment chemistries that are simple and reproducible.

Although many different types of surfaces have been used as substrates for DNA attachment, the need for reproducible, stable surfaces has placed increased emphasis on the preparation of DNA-modified surfaces that are extremely homogeneous. Recent studies have shown that crystalline silicon can be used as a starting point for preparing DNA layers exhibiting a high specificity and a high density of binding sites. Crystalline silicon has a number of potential advantages as a substrate for DNA immobilization. Perhaps more

importantly, the use of crystalline silicon substrates provides the potential for taking full advantage of existing microelectronic technologies associated with the silicon semiconductor industry, which can be used for highly parallel microfabrication and, in principle, direct electronic detection of biomolecular binding processes.

Recent experiments have shown that well-defined DNA layers can be prepared on the common (100) and (111) surfaces of silicon. In both cases, attachment was achieved by first using a long-chain alkene terminated with a reactive functional group[30, 31, 32]. While such long-chain molecules might provide improved stability against oxidation or other undesired reactions at the interface, it is also possible that such long-chain molecules might decrease the quality of the interface through entanglement. In emerging applications involving direct electronic detection of DNA hybridization processes, however, the use of a shorter linking layer may be beneficial. Ideally, one would like to identify the simplest chemical scheme for linking DNA to silicon substrates in a way that achieves the highest selectivity, sensitivity, and stability in subsequent hybridization steps.The best results will be a compromise in calibrating the length of linking chain. Infact, from one hand long chain improve stability at the expense of sensitivity, while from the other hand short chain reduce the stability of layers but increase sensitivity[1].

The (100) silicon surface is characterized by the binding of adjacent atoms,

[1]Electric interaction depends inversely from the distance.

with the consequent formation of ordered rows of dimers (Section 2.1). From a chemical point of view, the bonding within such a dimer is analogous to a localized double bond, involving four electrons in two orbitals strongly localized between the two Si atoms. This circumstance is of great interest because it suggests that the chemical reactivity of a surface dimer might be similar to that of an unsaturated organic molecule. In reality this is not completely true and in many cases it is possible to observe different reaction paths that have no analogous in solution reactions. An example of this case, that will be one of the main subject of this chapter, is the [2+2] cycloaddition reaction. In solution the reaction occurrs through a concerted mechanism that according to the Woodward-Hoffmann rules is symmetry forbidden. So it is required particular experimental conditions and long time to achieve equilibrium. On silicon surface the same reaction occurr at room temperature and in few minutes suggesting a different mechanism is involved. In particular, the presence of silicon bulk induce an anisotropy character breaking the symmetry and leading to a separation of charge in the dimer atoms giving a zwitterionic character to the dimer itself. In such a way, the reaction mechanism is completely different. As it will be shown later in this chapter, the mechanism more likely consists in the formation of a complex on the positively charged silicon dimer atom followed by the nucleophilic attack of the other silicon dimer atom.

As already mentioned there are many routes to the preparation of DNA-modified surface. Later on will be presented the route based on the addition

of a substituted cycloalkene (ACP, 1-amino-3-cyclopentene) to a Si-Si dimer, a reaction formally equivalent to a $[2+2]$ cycloaddition. In general, direct attachment of alkenes that also bear a primary amine group leads to poorly defined attachment. However, protecting the amine with the *tert*-butyl oxycarbonyl (t-BOC) group reduces the basicity of the amine and apparently also reduces or eliminates its oxidizing effect on the Si surface due to the presence of igroscopic water. By utilizing the protected amine, it is possible to prepare a surface with a high density of reactive amine groups. The molecule anchoring involves two directional bonds, resulting in organic layer that can be characterized by a high degree of order, both translational and orientational, leading to useful electronic and optical properties.

The resulting amine-terminated surfaces were covalently coupled to thio-oligonucleotides using a heterobifunctional crosslinker sulfo-succinimidyl 4-(N-maleimidomethyl) cyclohexane-1-carboxylate (SSMCC). Hybridization experiments revealed that these DNA/RNA modified surface exhibit excellent stability to hybridization conditions, high density and high specificity for recognition capable of identifying a single-base mismatch out of 16 bases[31].

2.1 Silicon Surface (100)-2x1

The (100)-2×1 Si surface is one of the most investigated surfaces both experimentally and theoretically because of its technological importance. Despite extensive studies, the nature of its reconstruction is still a subject of discussion both from experimental and theoretical perspectives. Recent studies by low-temperature scanning tunneling microscopy STM[33] raised a question on its ground state structure while the structure has also been discussed theoretically as a model surface at which so-called statical and dynamical electron correlations play subtle but significant roles on the structural determination. In particular, this types of electron correlation refer, respectively, to long range[34] and to short range correlation[35]. The former will tend to give symmetric dimer while the latter will tend to give asymmetric dimer.

On the surface, a dimer structure is formed for a reduction of the dangling bond density. The dimers are arranged linearly in the (110) direction to form a so-called ”dimer row” structure with a long-range 2×1 periodicity. The unique feature that leads the surface to show a variety of phases is a tilting or buckling of the dimer: the two dimer-composing atoms are located up and down relative to the surface plane. Along the dimer-row direction the asymmetric buckled dimer exhibits an ”antiferromagnetic”-like interaction to make a zigzag structure. Interaction between the neighboring dimer rows can be either ”ferromagnetic” or ”antiferromagnetic” producing a p(2×2) or

c(4×2) ordering, respectively. According to the generally accepted scenario on a temperature dependence of the structure , an order-disorder phase transition occurs at around 200 K; below the transition temperature the buckled dimers are arranged with the c(4×2) ordering, and above the temperature the thermally activated dimer flip-flop motion breaks the symmetry to exhibit the 2×1 ordering.

Figures 2.1 shows STM images taken at a temperature below 10 K with neg-

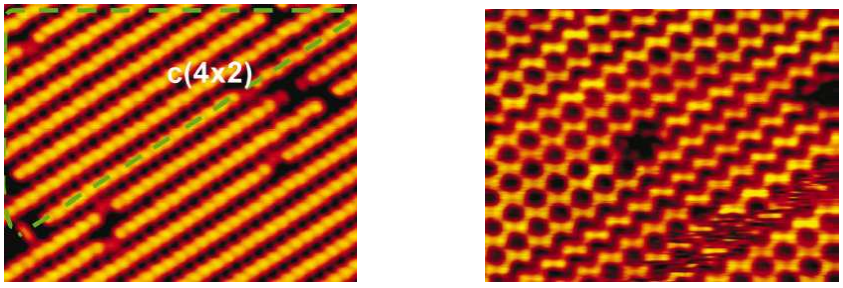

(a) Positive bias. (b) Negative bias

Figure 2.1: Color STM images of Si(100)2×1 surface taken below 10 K with a sample bias voltage of -2.2 V (a) and 1.6 V (b) (Taken from ref. [33]).

ative (a) and positive (b) sample bias voltages. Filled and empty electronic states of the sample surface around the Fermi level are imaged, respectively. The filled state image Fig. 2.1(a) shows equally spaced linear features, or dimer rows, running in the (110) direction. The linear feature is composed of the cocoon-shaped dimers. In the image most of the surface area is seem-

ingly covered with symmetric dimers. The empty state image, presented in Fig. 2.1(b), shows a remarkable contrast from its counterpart. Almost all area is filled with zigzag dimer rows, supporting for a presence of buckled dimers on the surface. Depending on a correlation of the zigzag pattern with the neighboring dimer rows, two types of ordering exist: in phase and out of phase, corresponding to p(2x2) and c(4x2) ordered structure, respectively. At a boundary of the phases a transitional motion of phase boundary is observed quite often as a fuzzy-looking region.

2.2 Computational Details

Part of the present work has been done in collaboration with Prof. Ninno group of the Departement of Physics of the University of Naples ”Federico II”, in order to compare our results obtained with GTO (Gaussian Type Orbitals) with their results obtained with PW (Plane Wave) methodologies. In both cases DFT (Density Functional Theory) were used. The calculations with Gaussian basis sets have been performed with the Gaussian 03 package[14], using DFT in the local density approximation (LDA) or in the generalized gradient approximation (GGA). In the latter case, we used the Perdew Burke Ernzerhof (PBE) functional[36] and its hybrid i.e., including a fixed amount of Hartree Fock exchange counterpart known as PBE0[37]. The all-electron basis sets ranged from split-valence (6-31G) to triple-zeta valence (6-311G), possibly augmented by polarization functions on all atoms [6-31G(d,p), 6-311G(d,p)] and by diffuse functions on non-hydrogen atoms [6-31+G(d,p), 6-311+G(d,p)]. In most calculations the inner electrons of all or part of silicon atoms are described by the CEP-31G[38] and the LANL2DZ[39] pseudopotentials, and the valence electrons by the related basis sets labeled by the same acronyms , possibly augmenting the LANL2DZ basis set by one set of *d* polarization functions and one set of *sp* diffuse functions referred to in the following as LANL2+(d). The total spin state was S = 0. Geometry optimizations were performed using the default Gaussian 03 convergence

thresholds on forces and on expected atom displacements which ensure a very reliable and robust search for minima and transition states. The nature of stationary points was always confirmed by computing second derivative eigenvalues. Reaction paths were drawn by locating the minima and the corresponding saddle points on the potential surface, then computing the intrinsic reaction coordinate (IRC) around the saddle point, and completing the curves with minimizations ending with the reactants and with the products, respectively. Analytical energy second derivatives were computed for all the stationary points in order to characterize them as minima or first order saddle points and to compute the temperature-dependent vibrational contributions to the free energy.

The calculations with plane waves have been performed using the ESPRESSO package[40], within the GGA approximation using the PBE density functional, ultrasoft pseudopotentials to describe the N, C, and H atoms, and a norm-conserving pseudopotential for the Si atom.

For studying the ACP molecule as well as the cluster models (Section 2.3.1) and the ACP-cluster complexes, the systems have been embedded in cubic supercells, containing enough space in order to prevent periodic replicas from interacting with each other. A careful analysis has been done to check the convergence of the obtained results with respect to the plane-wave basis set cutoff and the supercell side[41].

The reliability of these cluster models of the silicon (100) surface has been

checked by performing a set of surface calculations of adsorbed ACP on periodic, infinite silicon slabs. Periodic replicas of the slab are separated by empty space, equivalent to six silicon atomic layers. ACP molecules are adsorbed on both sides of the slab, thus preserving inversion symmetry about the center of the slab. This prevents the calculation from spurious effects arising from charge transfer between the two sides of the slab. The clean surface consists of rows of silicon dimers, for which different kinds of reconstruction are possible. Both 2×1 and 2×2 surface reconstructions have been considered, with a surface unit cell containing one or two dimers, respectively.

The ACP concentration on the surface has been varied from 1 (one adsorbed molecule per surface dimer) to 0.5 (one adsorbed molecule each for two dimers) to 0.25 monolayers (one adsorbed molecule each for four surface dimers) for checking how the relaxed geometries and the adsorption energy change from fully covered surfaces to isolated adsorbed molecules.

The GTO and PW approaches provide complementary information about the reaction paths on clusters and on periodic surfaces; when possible, we computed the same quantities (optimized geometrical parameters and relative energies) with both the approaches to cross-check the reliability of the results. Such a combined computational strategy is particularly important in this field that is intrinsically borderline between the molecular and the solid state theories.

2.3 Results

The cycloaddition mechanism has been recently experimented for attaching a number of organic molecules on the silicon (100) surface, using both wet and vacuum techniques[23].

Here has been considered a bifunctional molecule, 1-amino-3-cyclopentene (ACP; Fig. 2.2), possessing both a double bond able to react with the silicon dimer and an amino moiety available for further functionalizations, possibly leading to a more complex organic layering on the surface. Later on it has

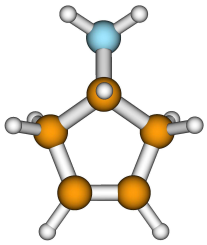

Figure 2.2: Geometrical structure of ACP.

been considered a computational study of these reactions considering both chemical functionalities.

2.3.1 Silicon Surface Model Systems

The model of the surface was prepared including the minimum number of features necessary to describe the chemical reaction of ACP on the surface. For the surface simulation were used cluster models that simulate the presence of just one dimer on the surface but with a different number of layers below it[42]. The clusters were partially hydrogenated to complete the tetrahedral environment around the surface silicon atoms that are not involved in the double bond. Using Si-H bonds to saturate the valences is a common practice, and it is justified by the strongly localized nature of the silicon bonding. The Si_9H_{12} cluster (Fig. 2.3) has been widely used in previous studies, because it is the smallest model with two atoms resembling the (100) surface. The larger cluster, with 29 silicon atoms (Fig. 2.4), is a more realistic model, in which five silicon atoms are bulklike, 12 atoms form six (100) surfaces, and the remaining 12 atoms belong to (111)-like faces.

In order to study the reconstruction process it has been considered the fully hydrogenated clusters, Si_9H_{16} (Fig. 2.3(a)) and $Si_{29}H_{36}$ (Fig. 2.4(a)), as well as the partially dehydrogenated models, Si_9H_{12} (Fig. 2.3(b)) and $Si_{29}H_{32}$ (Fig. 2.4(b)), where four hydrogens were removed from the (100) face to allow the formation of Si=Si double bond. The geometries of all the clusters were optimized with both Gaussian Type Orbitals and Plane Waves basis set functions at different levels of DFT theory. In Tables 2.1 and 2.2 are reported

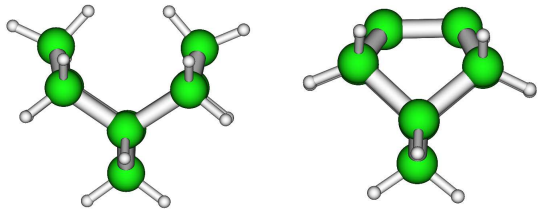

(a) Full hydrogenated surface cluster.

(b) Reconstructed cluster.

Figure 2.3: Relaxed geometries of (a) Si_9H_{16} and (b) Si_9H_{12} clusters.

the main geometrical parameters (see Figures 2.5 for geometrical parameters definition) referred to this process. After reconstruction, it is possible to observe an overall contraction of the surface atoms toward the bulk. GTO and PW optimizations show a remarkable agreement when the same functional is used in both methods, with the exception of the buckling angle. PW calculation provide much larger buckling angle than their GTO counterparts, with all the functionals and the basis sets. The silicon dimer buckling has been experimentally observed and studied by many authors, though its exact magnitude and origin are still being debated. This is a specific feature of surface silicon dimers; unlike in carbon double bonds, the energy is apparently lowered by breaking the symmetry between the two atoms, adding a zwitterionic character to the bond, with a partial negative charge on the outer silicon atom. Besides strengthening the bond, this charge separation increases the variety of organic reactions that can occur on the surface dimers, including some nucle-

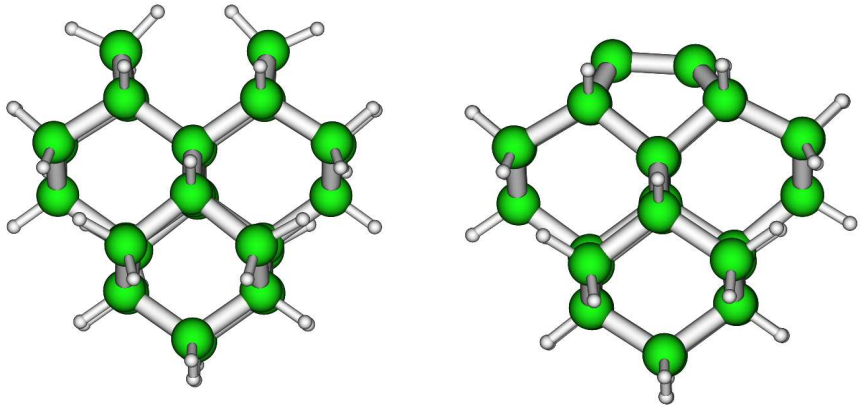

(a) Full hydrogenated surface cluster. (b) Reconstructed cluster.

Figure 2.4: Relaxed geometries of (a) $Si_{29}H_{36}$ and (b) $Si_{29}H_{32}$ clusters.

ophilic or electrophilic processes, as in the case analyzed in the next section (page 55).

Due to the chemical importance of the dimer tilting more investigations have been done to better understand the source of the differences between the optimized structures; from Tables 2.1 and 2.2 it is clear that the smaller angles obtained by the GTO calculations do not depend on the particular functional used. On the other hand, the $Si_{29}H_{32}$ cluster optimization at the Hartree Fock level with CEP-31G pseudopotentials provided a symmetric structure (with no tilting) a result in agreement with some previous multireference calculations, concluding that the dimer tilting could be a consequence of the introduction of dynamical correlation by DFT methods[43]. Basis set around the

Table 2.1: Main geometrical parameter for Si9 fully and partially hydrogenated clusters.

	Si_9H_{16}					
	PW		GTO			
Functional	LSDA	PBE	LSDA[a]	PBE[a]	PBE0[a]	PBE0[b]
Si(1)-Si(2)[c]	4.385	4.288	4.250	4.532	4.502	4.567
Si(2)-Si(3)	2.354	2.371	2.330	2.360	2.348	2.389
Si(3)-Si(2)-Si(4)	110.7	110.3	110.9	111.8	112.0	112.2
Si(2)-H(5)	1.496	1.497	1.501	1.502	1.492	1.516
	Si_9H_{12}					
	PW		GTO			
Functional	LSDA	PBE	LSDA[a]	PBE[a]	PBE0[a]	PBE0[b]
Si(1)-Si(2)	2.207	2.238	2.217	2.241	2.207	2.259
Si(2)-Si(3)	2.322	2.330	2.328	2.338	2.326	2.379
Si(3)-Si(2)-Si(4)	112.1	119.0	111.6	117.4	118.0	116.5
Buckling angle[d]	9.1	9.6	9.0	6.9	3.2	3.0

[a] 6-31+G(d,p) basis set.
[b] CEP-31G basis set.
[c] See figure 2.5 on page 49 for atom number definitions.
[d] See figure 2.5(d) on page 49 for Buckling angle definition.

surface dimer was also enlarged through the use of mixed basis set scheme. That is, starting from the PBE0/6-31+G(d,p) Si_{29} cluster structure, geometry has been reoptimized using the 6-311++G(2d,p) basis set on the two silicon atoms involved in the double bond, and then extending the larger basis to the four underlying silicon atoms. Both the optimizations resulted in structures similar to those already obtained, with buckling angles of 4.9° and 5.4°, respectively. Then the triplet ground state of the same cluster has been opti-

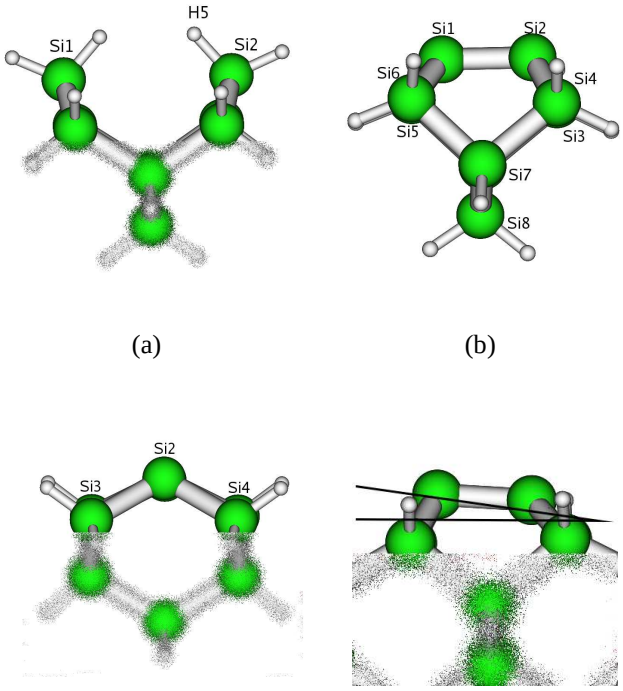

(a) (b)

(c) (d) Buckling angle definition.

Figure 2.5: Geometrical parameter number definitions.

mized at the PBE0/CEP-31G level. In this case the final geometry is perfectly symmetric, with no dimer tilting, indicating that the charge transfer between the two partners occurs through the π component of the bond. On this basis, one could argue that the smaller angles found with GTO are due to a mixing between singlet and triplet states; however, all the unrestricted singlet GTO calculations did not show any spin contamination. Our conclusion is that the PW approach tends to overestimate the charge transfer in the dimer with respect to GTO. On the other hand, the experimental data do not provide a clear indication about the size of the surface tilting. In Table 2.3 are reported more detailed geometrical parameters of reconstructed clusters obtained within GTO basis set finctions methods with three different DFT functionals that represent three different level of approximation: the local spin density approximation (LSDA)[44] that represent a very poor one based upon the uniformity of electron charge distribution; the PBE[36] functional belong to the generalized gradient approximation (GGA) family in which the exchange-correlation functional depends on the density gradient too so as to take into account of inhomogeneity in the electron density; the PBE0[37] hybrid functional, is like PBE but with the exchange part computed as exact Hartree-Fock and PBE exchange in the proportion 1:3. This functional represents a better description of the electron correlation with the approximate inclusion to some extent of both statical and dynamical correlation.

For all data reported in table 2.3 it was observed the typical trend expected

Table 2.2: Main geometrical parameter for Si_{29} fully and partially hydrogenated clusters.

	$Si_{29}H_{36}$					
	PW		GTO			
Functional	LSDA	PBE	LSDA[a]	PBE[a]	PBE0[a]	PBE0[b]
Si(1)-Si(2)[c]	4.101	4.187	4.097	4.194	4.176	4.242
Si(2)-Si(3)	2.327	2.360	2.333	2.365	2.353	2.398
Si(3)-Si(2)-Si(4)	109.2	108.9	109.3	109.2	109.2	109.2
Si(2)-H(5)	1.498	1.494	1.500	1.499	1.488	1.512
	Si_9H_{12}					
	PW		GTO			
Functional	LSDA	PBE[a]	LSDA[a]	PBE[a]	PBE0[a]	PBE0[b]
Si(1)-Si(2)	2.275	2.268	2.270	2.259	2.258	2.269
Si(2)-Si(3)	2.341	2.343	2.337	2.347	2.335	2.396
Si(3)-Si(2)-Si(4)	116.1	116.2	115.9	115.0	115.2	113.3
Buckling angle[d]	15.8	15.7	11.2	9.0	4.8	4.7

[a] 6-31+G(d,p) basis set.
[b] CEP-31G basis set.
[c] See figure 2.5 on page 49 for atom number definitions.
[d] See figure 2.5(d) on page 49 for Buckling angle definition.

for the use of these functionals, thas is, starting from the LSDA lengths, PBE gave longer values, while the inclusion of nonlocal correction in PBE0 shorten bond lengths[45]. Nevertheless, this trend did not apply to the silicon dimer bond length reflecting the much more complex situation from the electron structure point of view. In fact, in the literature there are a lot of discrepancies about the exact picture of silicon dimer bond in terms of which it could be represented as the hybrid constituted from a π, dangling bond and zwitterionic characters, that can be expressed schematically as:

$$Si = Si \longleftrightarrow \dot{S}i - \dot{S}i \longleftrightarrow Si^{-} - Si^{+}$$

The PBE0 functional, due to the nature of HF exchange contribution[2], take into account of the parallel spin correlation in a better way. Consequently, the density redistribute through the silicon dimer atoms region in corrispondence of bond causing a more shielding between such a atoms. The decreased nuclear repulsion could explain the shorter bond lengths observed. The basis set used, 6-31+G(d,p), was enough extended, with the inclusion of polarization and diffuse function, to gave a good description of these effects. Comparing these bond lenghts to the correnspondingbuckling angles it is possible to notice a direct proportionality between these quantities, consequenly for PBE0 model it was found a less separation of charges on silicon dimer supporting

[2]The exchange energy can be considered simply as some sort of correlation between electron with the same spin that arise from the antisymmetry requirement of the wave function through the Slater determinat.

this picture.

From the chemical point of view, however, the relevant information is that

Table 2.3: Si_9H_{12} and $Si_{29}H_{32}$ geometrical parameters obtained with different DFT functionals and 6-31+G(d,p) basis set.

Geometrical	*Si*$_9$*H*12			$Si_{29}H_{32}$		
Parameter[a]	LSDA	PBE	PBE0	LSDA	PBE	PBE0
Si1-Si2	2.217	2.240	2.207	2.248	2.273	2.246
Si1-Si3	2.308	2.336	2.326	2.320	2.348	2.334
Si2-Si5	2.328	2.355	2.333	2.347	2.380	2.363
Si3-Si7	2.341	2.373	2.360	2.342	2.375	2.361
Si5-Si7	2.339	2.370	2.359	2.340	2.374	2.360
Si7-Si8	2.341	2.375	2.364	2.360	2.401	2.387
Si3-H1	1.500	1.501	1.490	1.504	1.506	1.494
Si3-H2(Si9)[b]	1.499	1.501	1.490	2.325	2.356	2.344
Si1-Si2-Si5	97.2	99.7	103.8	92.4	93.2	93.9
Si2-Si1-Si3	85.7	112.7	109.6	118.5	118.1	117.7
Si3-Si1-Si4	117.6	117.4	118.0	116.4	116.4	116.9
Si5-Si2-Si6	111.8	117.5	115.7	106.4	106.8	107.4
Si1-Si3-Si7	89.8	91.0	92.7	85.9	86.4	86.6
Si2-Si5-Si7	102.7	100.7	115.7	106.1	105.5	104.9
Si3-Si7-Si8	108.1	108.4	108.6	107.1	107.0	106.9
Si5-Si7-Si8	108.9	108.7	108.8	106.6	106.8	106.9
Si1-Si3-H1	114.8	114.9	114.3	113.2	113.2	113.1
Si1-Si3-H2(Si9)[a]	113.1	112.8	112.4	116.2	116.1	115.7
Si3-H1-H2(Si9)[a]	109.9	109.2	109.1	114.3	113.7	113.7
Si3-Si1-Si2-Si5	13.2	10.1	4.8	22.0	21.0	20.5
Buck. Angle	9.0	6.9	3.3	14.4	13.8	13.4

[a] For definitions about these parameters see figures 2.5 on page 49.

[b] This parameter will be Si3-H2 for Si_9H_{12} and Si3-Si9 for the larger $Si_{29}H_{32}$ cluster model.

some asymmetry exists inside the silicon double bond, and that the resulting

zwitterionic character influences the course of the addition reaction, as it will be shown in the next section.

Finally, the charge difference between the dimer silicon atoms in both clusters was computed by fitting the electrostatic potential on all the optimized structures. A clear relation exists between the buckling angle and the charge difference, ranging from 1.54 a.u. when the angle is 3.0°, as in Si_9H_{12} optimized at the PBE0/CEP-31G level, to 4.56 a.u. in $Si_{29}H_{32}$ optimized with plane waves PBE functional , where the angle is 14.7°; in all the cases the inner silicon atom is more positive, that is, more suitable for nucleophilic attacks[40].

2.3.2 ACP Reactions

Direct attachment of ACP leads to chemically heterogeneous surfaces, while the use of suitable protection and deprotection chemistry can produce a homogeneous surface with a high density of primary amino groups suitable for further functionalizations.

The reaction of ACP on Silicon surface model systems was investigated for both its chemical functionalities, that is, double bond and amino group.

In both cases the reactions proceed through the formation of an initial intermediate complex followed by the formation of the final product through a transition state. The structures of the intermediates , the transition states , and the products for both clusters and both reactions are drawn, respectively, in Figures 2.6 and 2.7.

In tables 2.4 and 2.6 the SCF energies for both reaction paths and clusters are reported, while in tables 2.5 and 2.7 are reported the corresponding Gibbs Free energies at 298 K and 1 atm obtained within the formalism of partition function. In figure 2.8 the graphical representation of both reaction coordinates is depicted so as to give a more intuitive picture of the reactions involved.

This calculations are consistent with experimental observations of competing reactions. Infact, it is evident from the data showed in these tables that both reactions can effectively compete at the surface reaction sites producing an inhomogeneous surface. In particular, it would seem that the double bond

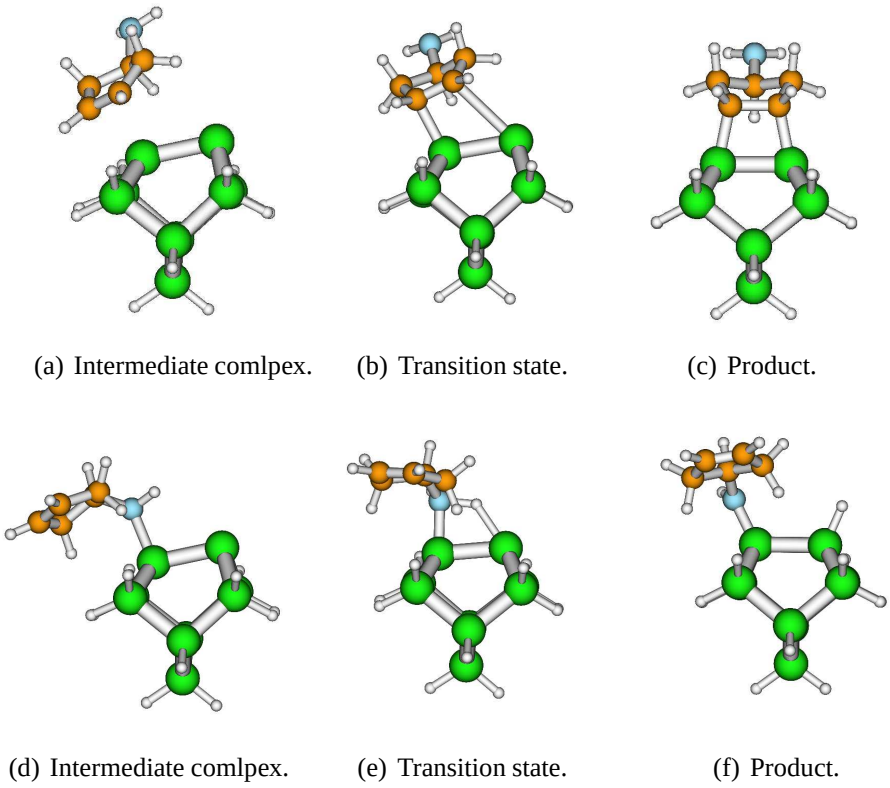

(a) Intermediate comlpex. (b) Transition state. (c) Product.

(d) Intermediate comlpex. (e) Transition state. (f) Product.

Figure 2.6: Stationary point of the Potential energy surface of Si_9H_{12} reaction with ACP, through both double bond (a-c) and amino group (d-f).

pathway is preferred kinetically while the amino group pathway instead is preferred thermodynamically. In the case of attachment through amino group both intermediate and product are thermodinamically more stable, while the kinetic barrier is lower in double bond reaction path. So the free reaction of ACP on silicon surface produce not reproducible surface with no technological applications.

In tables 2.8, 2.9, 2.10 and 2.11 are reported the main geometrical parame-

Table 2.4: SCF energy profile of ACP reaction on Si_9H_{12} and $Si_{29}H_{32}$ clusters through double bond without ZPE correction.All data are reported in $kcal mol^{-1}$

	Basis Set	ΔE_{int}	ΔE_{TSadd} [a]	ΔE_{prod}
Si_9H_{12}	CEP-31G	-15.10	-8.29(6.81)	-52.09
	LANL2DZ	-9.35	-4.51(4.84)	-54.29
	Mixed basis[b]	-16.54	-10.97(5.57)	-55.47
$Si_{29}H_{32}$	CEP-31G	-14.40	-8.67(5.73)	-51.44
	LANL2DZ	-10.94	-6.83(4.11)	-55.57
	Mixed basis[b]	-17.81	-12.79(5.02)	-56.82

[a] Barriers are reported in pharenthesis.
[b] 6-31G* on ACP and silicon dimer, LANL2DZ elsewhere.

Table 2.5: Gibbs Free energy profile at 298 K and 1 atm of ACP reaction on Si_9H_{12} and $Si_{29}H_{32}$ clusters through double bond.All data are reported in $kcal mol^{-1}$

	Basis Set	ΔF_{int}	ΔF_{TSadd} [a]	ΔF_{prod}
Si_9H_{12}	CEP-31G	-1.05	5.88(6.93)	-35.48
	LANL2DZ	3.67	9.09(5.42)	-38.23
	Mixed basis[b]	-2.22	3.55(5.77)	-38.97
$Si_{29}H_{32}$	CEP-31G	-1.89	4.66(6.55)	-35.68
	LANL2DZ	2.44	7.33(4.89)	-38.89
	Mixed basis[b]	-4.37	1.19(5.56)	-41.06

[a] Barriers are reported in pharenthesis.
[b] 6-31G* on ACP and silicon dimer, LANL2DZ elsewhere.

Table 2.6: SCF energy profile of ACP reaction on Si_9H_{12} and $Si_{29}H_{32}$ clusters through amino group without ZPE correction.All data are reported in $kcalmol^{-1}$

	Basis Set	ΔE_{int}	ΔE_{TSadd} [a]	ΔE_{prod}
Si_9H_{12}	CEP-31G	-35.66	-15.11(20.54)	-52.01
	LANL2DZ	-32.67	-24.78(16.36)	-55.25
	Mixed basis[b]	-43.47	-24.78(18.70)	-69.31
$Si_{29}H_{32}$	CEP-31G	-35.26	-14.34(20.92)	-48.88
	LANL2DZ	-34.85	-18.03(16.82)	-56.20
	Mixed basis[b]	-55.73	-36.88(18.85)	-80.71

[a] Barriers are reported in pharenthesis.
[b] 6-31G* on ACP and silicon dimer, LANL2DZ elsewhere.

Table 2.7: Gibbs Free energy profile at 298 K and 1 atm of ACP reaction on Si_9H_{12} and $Si_{29}H_{32}$ clusters through amino group.All data are reported in $kcalmol^{-1}$

	Basis Set	ΔF_{int}	ΔF_{TSadd} [a]	ΔF_{prod}
Si_9H_{12}	CEP-31G	-20.24	-3.27(16.98)	-38.72
	LANL2DZ	-17.73	-4.97(12.76)	-43.59
	Mixed basis[b]	-26.72	-12.62(14.09)	-56.78
$Si_{29}H_{32}$	CEP-31G	-20.22	-3.74(16.49)	-37.75
	LANL2DZ	-19.16	-6.24(12.92)	-44.07
	Mixed basis[b]	-37.61	-23.12(14.49)	-66.14

[a] Barriers are reported in pharenthesis.
[b] 6-31G* on ACP and silicon dimer, LANL2DZ elsewhere.

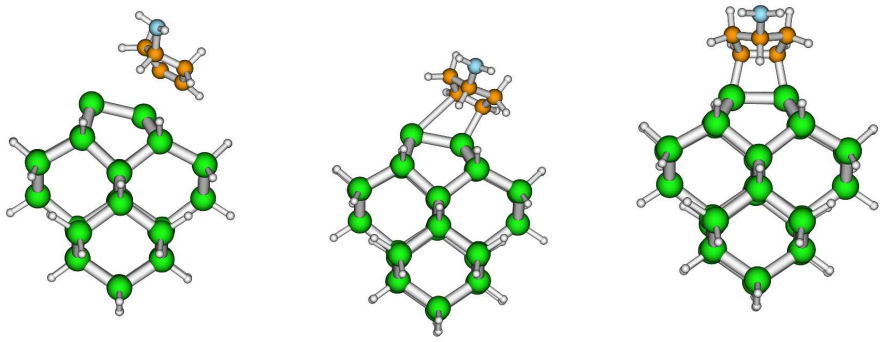

(a) Intermediate comlpex. (b) Transition state. (c) Product.

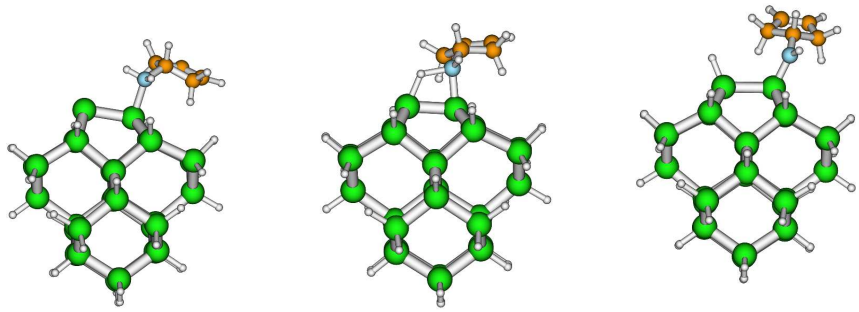

(d) Intermediate comlpex. (e) Transition state. (f) Product.

Figure 2.7: Stationary point of the Potential energy surface of $Si_{29}H_{32}$ reaction with ACP, through both double bond (a-c) and amino group (d-f).

ter referred to both reaction paths considered on both cluster model systems. Different GTO basis set function were considered and are denoted as: CEP for CEP-31G; LANL2 for LANL2DZ and mixed stands for 6-31G(d,p) basis set on ACP and silicon dimer while LANL2DZ elsewhere.

It is possible to observe that in both reactions there is a tendency toward the

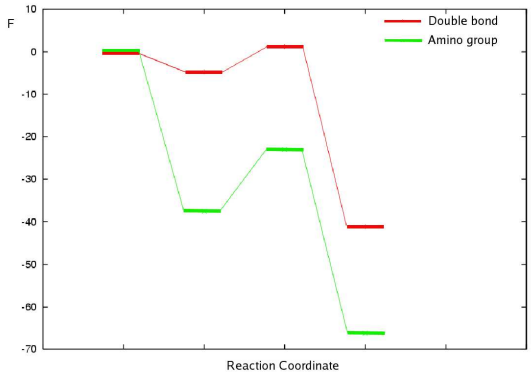

Figure 2.8: Graphical representation of reaction paths through both ACP functionality

saturation of the silicon dimers. That is, the surface tends to ”debuckling” through the direction of symmetric silicon dimers. In every cases studied it has been observed a buckling angle of exactly 0.0 for the double bond reaction products while a very near to zero value for the amino group reaction products (about 1°).

In the following, since the general trends remain the same for every basis set tabulated, for the sake of simplicity it will be exposed only the mixed basis set[3] numerical value on $Si_{29}H_{32}$ cluster.

The silicon dimer bond length during the reactions evolves through values much more close to the bulk parameters. The bond length start from the value of 2.212 to the value of 2.353 Å close to 2.379 Å of the Si7-Si9 bond length that has a bulk character. This can be explained according to the change in

[3]For the geometrical parameters defi nition see Figures 2.9 and 2.5(d) on pages 62 and **??**.

orbitals hybridization from sp^2 to sp^3 as expected.

In the case of ACP double bond path an analogous behaviour in which it is possible to observe a parallel lengthening of the bond together with the concomitant change in bond angle. The C1-C2 bond length pass from 1.334 to 1.586 Å while the bond angle C1-C2-H2 go from 125.3 to 101.0°, very near to tetrahedral geometry. The carbon atoms of ACP move closer to the silicon dimer as it clear following the Si2-C2 bond length that reduce from 3.515 to 1.948 Å. Considering the C1-C2-Si1-Si2 dihedral angle results that the double bond in ACP molecule turn of about 30° reaching a perfectly aligned configuration with the silicon dimer in the final summetric product.

In the case of amino group path, concerning the silicon clusters the story remain exactly the same, a lengthening of silicon dimer bond from 2.212 to 2.404 Å were observed. The Si1-N1 bond length shorten going from 1.992 to 1.739 Å in parallel with one of the hydrogen atom bound to the nitrogen move away breacking the bond going from 1.018 to 3.721 Å.

In general the intermediary character of the geometrical parameters going from the complex formation to the product give a further confirmation that the transition state found really connect the reactants with product. This statement has corroborated further with the computation of analytical frequencies. From the analysis of the Hessian eigenvalue it has been possible not only to characterize the nature of saddle points of Potential Energy Surface (PES),

that for transition state it must be of first order [4] but observing the normal mode corresponding to the imaginary frequency it is possible to follow directly the motion along this normal mode and check if it matches with the supposed reaction coordinate.

To check further the correctness of the stationary points found Intrinsic Reaction Coordinate (IRC) calculations were performed starting from the transition state geometry.

Furthermore, in both reaction paths the buckling angle increase before can-

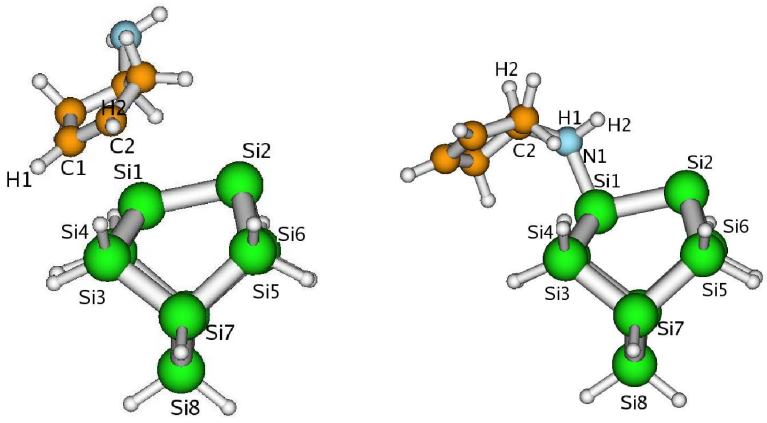

(a) Double bond path atom numbering.

(b) Amino group path atom numbering.

Figure 2.9: Atom numbering needed for geometrical parameters definition.

[4] A first order saddle point consists of a stationary point on an hypersurface that is minima for each coordinates except one for which it is a maximum and the eigenvalue is negative. So, in the case that physically such an eigenvalue is the square of a frequency, as in the present case, we have formally imaginary frequency.

cellation. Considering the correlation between the charge separation in the dimer and the buckling angle[5] it is possible to argue that the effect of complex formation, in both cases, is to promote the product formations in two ways. From one hand, there is an increasing of the nucleophilic character of the up silicon dimer atom. From the other hand, the ACP molecule at this point is bound on the surface in both cases, so due to the close proximity to such a silicon atom the reactions are statistically facilitated. The combination of both aspects could take into account the experimental observation that these reactions occur much more easily than the corresponding analogous concerted reactions in solution that are symmetry forbidden according to Woodward-Hoffmann rules.

Since in common practice the reaction path through the amino group is forbidden by the use of a suitable protection group scheme reactions, in the following more sophisticated techniques were considered for only the reaction path through the double bond. In particular, it has been reported a comparative study between GTO and PW basis set functions and further refinements of electronic representation on selected fixed geometry. These refinements consist in the extention of the basis set in a mixed scheme as in the previous section (Section 2.3.1), but here the addition of the extended basis set covers the ACP molecule too. Furthermore, basis set superposition error (BSSE) computed with the counterpoise method[46, 47] has been also included for

[5]The buckling angle increase with charge separation.

Geometrical	Reactants			Intermediate			TS			Product		
Parameter	CEP	LANL2	Mixed	CEP	LANL2	Mixed	CEP	LANL2	Mixed	CEP	LANL2	Mixed
Si1-Si2	2.260	2.204	2.212	2.447	2.374	2.355	2.414	2.370	2.352	2.442	2.401	2.392
Si1-Si3	2.378	2.335	2.327	2.407	2.354	2.354	2.393	2.345	2.343	2.407	2.363	2.356
Si2-Si5	2.390	2.335	2.349	2.458	2.392	2.389	2.412	2.364	2.364	2.398	2.352	2.350
Si3-Si7	2.417	2.369	2.368	2.392	2.348	2.347	2.402	2.355	2.355	2.392	2.344	2.347
Si5-Si7	2.417	2.369	2.364	2.407	2.357	2.358	2.405	2.356	2.357	2.394	2.347	2.348
Si7-Si9	2.419	2.369	2.363	2.401	2.353	2.350	2.406	2.357	2.354	2.400	2.350	2.348
Si3-Si1-Si4	116.5	114.5	115.1	105.9	106.7	105.0	109.9	109.9	108.7	104.2	104.0	103.1
Si5-Si2-Si7	114.1	114.4	110.5	94.9	97.6	96.4	104.2	104.2	103.5	104.6	104.8	104.3
Si1-N1	-	-	-	2.027	1.979	1.983	1.910	1.882	1.870	1.781	1.795	1.739
N1-H1	1.018	1.014	1.018	1.029	1.027	1.023	1.028	1.025	1.021	1.016	1.012	1.012
N1-H2	1.018	1.014	1.018	1.033	1.033	1.028	1.495	1.446	1.423	3.850	3.781	3.748
N1-C2	1.472	1.464	1.457	1.516	1.510	1.492	1.492	1.486	1.468	1.472	1.465	1.450
Si2-H2	-	-	-	-	-	-	1.785	1.801	1.823	1.517	1.492	1.493
Si1-Si2-H2	-	-	-	-	-	-	64.7	63.8	62.5	113.4	113.1	113.6
N1-Si1-Si2	-	-	-	100.2	99.9	101.1	84.5	85.3	86.7	116.7	110.9	115.2
Si1-N1-H1	-	-	-	103.6	104.5	103.8	111.8	110.5	111.8	117.4	117.9	115.8
Buck. Angle	3.0	0.1	6.6	10.0	8.1	9.1	4.8	4.3	4.9	0.8	0.9	1.1

Table 2.8: Main geometrical parameter of the ACP adsorbtion through amino group on Si_9H_{12} cluster. The parameter are expressed in Å or ° depending of the number of atoms defining the parameter. The definition of buckling angle are given in figure 2.5(d) on page 49, while the nubering are defined in 2.9(b) on page 62.

Geometrical	Reactants			Intermediate			TS			Product		
Parameter	CEP	LANL2	Mixed	CEP	LANL2	Mixed	CEP	LANL2	Mixed	CEP	LANL2	Mixed
Si1-Si2	2.260	2.204	2.212	2.491	2.417	2.402	2.490	2.444	2.409	2.387	2.344	2.326
Si1-Si3	2.378	2.335	2.327	2.404	2.353	2.356	2.408	2.356	2.356	2.393	2.348	2.347
Si2-Si5	2.390	2.335	2.349	2.471	2.404	2.400	2.450	2.393	2.384	2.393	2.348	2.347
Si3-Si7	2.417	2.369	2.368	2.390	2.345	2.344	2.391	2.344	2.344	2.403	2.356	2.357
Si5-Si7	2.417	2.369	2.364	2.405	2.356	2.358	2.399	2.350	2.349	2.403	2.356	2.357
Si7-Si9	2.419	2.369	2.363	2.398	2.351	2.348	2.398	2.350	2.348	2.410	2.361	2.358
Si3-Si1-Si4	116.5	114.5	115.1	104.9	105.7	103.6	105.8	106.4	105.3	109.2	109.0	108.7
Si5-Si2-Si7	114.1	114.4	110.5	93.9	96.8	95.4	96.5	98.2	98.2	109.2	109.0	108.7
Si1-C1	-	-	-	2.442	2.376	2.339	2.121	2.098	2.066	1.982	1.955	1.946
Si2-C2	-	-	-	3.638	3.553	3.523	3.004	3.020	2.909	1.982	1.955	1.946
C1-C2	1.364	1.347	1.334	1.404	1.391	1.381	1.440	1.425	1.417	1.602	1.596	1.588
C1-H1	1.091	1.086	1.087	1.091	1.087	1.087	1.093	1.088	1.089	1.102	1.096	1.095
C2-H2	1.091	1.086	1.087	1.091	1.087	1.088	1.090	1.085	1.086	1.102	1.096	1.095
C1-C2-H1	125.4	125.3	125.3	124.7	124.6	124.6	119.9	120.8	120.1	111.9	111.9	111.9
C1-Si1-Si2	-	-	-	125.6	124.9	127.2	108.2	112.0	111.1	78.6	79.0	79.1
Si1-Si2-C1-C2	-	-	-	148.1	147.1	117.0	-6.9	-9.0	-8.8	0.0	0.0	0.0
Buck. Angle	3.0	0.1	6.6	10.4	8.6	9.1	8.4	7.2	7.4	0.0	0.0	0.0

Table 2.9: Main geometrical parameter of the ACP adsorbtion through double bond on Si_9H_{12} cluster. The parameter are expressed in Å or ° depending of the number of atoms defining the parameter. The definition of buckling angle are given in figure 2.5(d) on page 49, while the nubering are defined in 2.9(a) on page 62.

Geometrical	Reactants			Intermediate			TS			Product		
Parameter	CEP	LANL2	Mixed	CEP	LANL2	Mixed	CEP	LANL2	Mixed	CEP	LANL2	Mixed
Si1-Si2	2.270	2.204	2.212	2.467	2.399	2.376	2.424	2.380	2.359	2.459	2.418	2.404
Si1-Si3	2.384	2.335	2.327	2.415	2.360	2.359	2.399	2.349	2.347	2.422	2.373	2.371
Si2-Si5	2.397	2.335	2.349	2.459	2.395	2.390	2.416	2.367	2.366	2.401	2.352	2.350
Si3-Si7	2.421	2.369	2.368	2.409	2.359	2.359	2.413	2.362	2.362	2.399	2.349	2.351
Si5-Si7	2.419	2.369	2.364	2.408	2.355	2.357	2.416	2.362	2.364	2.402	2.351	2.353
Si7-Si9	2.450	2.369	2.363	2.425	2.372	2.369	2.435	2.382	2.378	2.424	2.371	2.367
Si3-Si1-Si4	116.5	114.5	115.1	108.9	109.5	108.1	111.9	111.9	110.8	107.1	103.9	106.1
Si5-Si2-Si7	114.1	114.4	110.5	98.8	100.9	100.1	108.2	106.7	105.9	107.5	107.7	107.3
Si1-N1	-	-	-	2.038	1.990	1.992	1.912	1.884	1.871	1.781	1.758	1.739
Si2-H2	-	-	-	2.938	2.863	2.890	1.779	1.794	1.817	1.519	1.494	1.495
N1-H1	1.018	1.014	1.018	1.029	1.026	1.023	1.027	1.024	1.020	1.016	1.012	1.012
N1-H2	1.018	1.014	1.018	1.034	1.034	1.029	1.506	1.454	1.430	3.807	3.744	3.721
N1-C2	1.472	1.464	1.457	1.515	1.510	1.491	1.492	1.486	1.468	1.472	1.465	1.451
Si1-Si2-H2	-	-	-	-	-	-	64.7	63.9	62.6	112.0	111.9	112.6
N1-Si1-Si2	-	-	-	97.8	98.4	99.1	84.4	85.1	86.4	115.7	115.7	115.0
Si1-N1-H2	-	-	-	100.4	99.9	100.4	84.3	84.4	83.3	61.3	61.2	61.9
Buck. Angle	4.9	3.9	5.9	9.7	8.2	9.0	4.7	4.3	5.0	0.9	0.9	1.1

Table 2.10: Main geometrical parameter of the ACP adsorbtion through amino group on $Si_{29}H_{32}$ cluster. The parameter are expressed in Å or ° depending of the number of atoms defining the parameter. The definition of buckling angle are given in figure 2.5(d) on page 49, while the nubering are defined in 2.9(b) on page 62.

the complex formation [6].

In table 2.12 are reported the main geometrical parameters for the ACP product on silicon clusters. In particular, it has been used PBE functional for PW basis set, while PBE0 model for GTO functions. In the latter case an effective core potential (ECP)[48, 49] basis set was used on cluster atoms except on silicon dimer and organic moiety (ACP) in which an extended all electron basis set with diffuse and polarization functions was used. This strategy allows to give a satisfactory electronic description of the center of reaction and at the same time take advantage of pseudopotentials [7].

[6] This error arise when a supermolecule is formed by the aggregation of smaller molecules. For example, considering the general reaction:

$$A + B \rightarrow AB$$

due to indistinguishability of electrons the basis set used to describe A and B species superimpose to describe AB. Than, this separated basis set will be smaller than that of AB. So the description of AB will be at a higher level with respect to the reactant introducing an error (BSSE). In order to take into account this error, in terms of counterpoise method, the energy barrier will be computed as:

$$\Delta E_{AB} = \left[E_{AB}^{AB}(A) + E_{AB}^{AB}(B) - E_{AB}^{AB}(AB)\right] + \left[E_{A}^{A}(A) + E_{B}^{B}(B) - E_{AB}^{A}(A) - E_{AB}^{B}(B)\right]$$

where $E_Y^Z(X)$ means the energy of system X, at geometry Y and with basis set Z. In such a way it is possible to avoid the above mentioned error.

[7] Briefly, pseudopotentials consist in the representation of the core electrons with simplified functions with respect to all electron models. This simplified functions are parameterized

Geometrical	Reactants			Intermediate			TS			Product		
Parameter	CEP	LANL2	Mixed	CEP	LANL2	Mixed	CEP	LANL2	Mixed	CEP	LANL2	Mixed
Si1-Si2	2.260	2.204	2.212	2.523	2.458	2.431	2.502	2.459	2.418	2.396	2.349	2.353
Si1-Si3	2.378	2.335	2.327	2.412	2.359	2.359	2.418	2.363	2.362	2.398	2.352	2.350
Si2-Si5	2.390	2.335	2.349	2.478	2.414	2.404	2.455	2.396	2.386	2.398	2.352	2.350
Si3-Si7	2.417	2.369	2.368	2.394	2.345	2.345	2.396	2.344	2.345	2.413	2.361	2.364
Si5-Si7	2.417	2.369	2.364	2.407	2.355	2.356	2.401	2.348	2.349	2.413	2.361	2.364
Si7-Si9	2.419	2.369	2.363	2.421	2.369	2.365	2.422	2.370	2.368	2.436	2.383	2.379
Si3-Si1-Si4	116.5	114.5	115.1	108.8	109.2	107.6	109.5	110.0	108.8	110.6	110.8	110.1
Si5-Si2-Si7	114.1	114.4	110.5	94.2	99.3	98.6	99.7	101.2	101.2	110.6	110.8	110.1
Si1-C1	-	-	-	2.457	2.387	2.348	2.151	2.123	2.088	1.986	1.957	1.948
Si2-C2	-	-	-	3.639	3.549	3.515	3.046	3.054	2.949	1.986	1.957	1.948
C1-C2	1.364	1.347	1.334	1.403	1.392	1.380	1.434	1.421	1.412	1.600	1.594	1.586
C1-H1	1.091	1.086	1.087	1.091	1.087	1.088	1.094	1.089	1.089	1.102	1.096	1.095
C2-H2	1.091	1.086	1.087	1.091	1.087	1.088	1.090	1.086	1.086	1.102	1.096	1.095
C1-C2-H1	125.4	125.3	125.3	124.7	124.7	124.6	120.2	120.9	120.4	112.0	111.9	101.0
C1-Si1-Si2	-	-	-	125.0	125.0	126.5	107.7	111.4	110.6	78.4	78.9	79.0
C1-C2-Si1-Si2	-	-	-	149.9	149.8	150.1	173.2	170.9	170.5	180.0	180.0	180.0
Buck. Angle	4.9	3.9	5.9	10.5	8.9	9.3	8.5	7.5	7.7	0.0	0.0	0.0

Table 2.11: Main geometrical parameter of the ACP adsorbtion through double bond on $Si_{29}H_{32}$ cluster. The parameter are expressed in Å or ° depending of the number of atoms defining the parameter. The definition of buckling angle are given in figure 2.5(d) on page 49, while the nubering are defined in 2.9(a) on page 62.

On these optimized structures, the potential energies have been computed at the PBE0 level with different basis sets, as indicated in tables 2.13 and 2.14, includeing the already mentioned BSSE and vibrationsl corrections. The latter correction has been computed at the same level used for the optimizations and simply added to the various potential energies. The potential energies of the stationary points with respect to the isolated reactants are reported in tables 2.13 and 2.14, along with an estimate of the corresponding free energies. It is worth noting that the shape of the reaction profile is very similar for Si_9H_{12} and $Si_{29}H_{32}$ clusters, especially when extended basis sets are used. The main differences between the reaction profiles on the two clusters concern the product stability with respect to reactants. They are about 6% more stable in $Si_{29}H_{32}$, and the activation barrier from the pre-reaction complex and the product is about $3\% - 6\%$ lower in $Si_{29}H_{32}$; anyway, such differences are quite small, especially when thermal corrections are included, and they do not change the profiles significantly. This confirms that the cycloaddition reaction is strongly local, and involves the two silicon atoms forming the surface dimer much more than the underlying layers. In Figures 2.10 and 2.11 are sketched the Highest Occupied Molecular Orbital (HOMO) and the Lowest Unoccupied Molecular Orbital (LUMO) for both clusters. As it is possible to observe they are localized near the surface in corrispondence of silicon dimer confirming the above mentioned invariance due to the fact that the underlying

so as to reproduce reference data often including relativistic effect too.

bulk induce little perturbation to the electronic state even though some steric interection in the larger cluster are noticeable.

The data collected in tables 2.13 and 2.14 clearly show that the formation energies of the pre-reaction complex ($\Delta E_{compl}, \Delta G_{compl}$) are poorly described with the standard valence basis sets related to pseudopotentials; the electrophilic interaction between the molecular π system and the positive end of the surface Si dimer needs a better valence basis set to be properly computed. On the other hand, this energy is not very sensitive to the size of the all-electron basis. A similar comment can be made about the product energies ($\Delta E_{prod}, \Delta G_{prod}$) , ruling the thermodynamics of the adsorption reaction. Because this quantity is formally related to the breaking of a C-C and a Si-Si π bond and to the formation of two σ Si-C bonds, it is not surprising that a flexible and more accurate basis set is required at least around the reactive center. It is very interesting, on the other hand, that the activation barrier ($\Delta E^{\ddagger}, \Delta G^{\ddagger}$) is much less sensitive to the choice of pseudopotentials and basis sets, even though the absolute energy ($\Delta E_{TS}, \Delta G_{TS}$) of the transition state depends on the calculation level markedly. The PW energy with respect to reactants for the Si_9H_{12}-ACP adduct (computed with the GGA functional with cutoff of 30 Ry and supercell side of 40 a.u.) is -39.4 kcal/mol (-1.710 eV) . On increasing the cut-off up to 50 Ry no variations are found for this energy. The same calculations done on the $Si_{29}H_{32}$-ACP cluster (40 a.u. supercell) gives -40.2 kcal/mol (1.744 eV) with a 30-Ry cutoff and -40.1 kcal/mol (1.739 eV) with

a 50-Ry cutoff.

In order to perform GTO calculations in about the same conditions as their PW counterparts, it has been recomputed ΔE_{prod} with the PBE functional and the largest basis set 6-311+G(d,p) on the silicon dimer and ACP using PW geometries and including the counterpoise correction to the BSSE; the result is -41.8 kcal/mol for the small cluster and -43.3 kcal/mol for the large cluster. The agreement with PW computations differences of about 5% can now be considered satisfactory in view of the different computational conditions e.g., pseudopotentials . Using the same large basis set, it has been finally obtained the best estimates, in the limits of present work, of thermodynamic and kinetic parameters governing the reaction using the PBE0 functional (Tables 2.13 and 2.14, last rows). Activation free energies barriers of 6.3 and 6.0, and reaction free energies of -36.4 and -39.8 kcal/mol for the Si_9H_{12} and $Si_{29}H_{32}$ cluster, respectively, have been found. Thus the cluster dimensions play a negligible role concerning the kinetics of the reaction, whereas this is not the case for the thermodynamics.

As already pointed out, PW calculations have been performed also for the ACP adsorption on infinite silicon (100) surfaces. This can give a significant check of the cluster model discussed previously. Different coverages of the surface have been considered for bringing out the effect of the surface density of adsorbed molecules on the main structural and electronic properties. This coverage is changed along the dimer rows. Indeed, the distance between two

neighbour dimers in the same row is calculated to be 3.872 Å, while it is 7.743 Å for two neighbour dimers belonging to different rows. The adsorption energy was calculated as

$$E_{ads} = -E_{prod} = -\frac{[E(surface + ACP) - E(surface) - nE(ACP)]}{n}$$

where n is the total number of ACP molecules in the unit cell. Three different coverages are considered here: (i) 1 monolayer (ML) , with one adsorbed molecule per surface dimer (2x2 unit cell, n = 4) ; (ii) 0.5 ML, with one adsorbed molecule each for two surface dimers (2x2 unit cell, n = 2); and (iii) 0.25 ML, with one adsorbed molecule each for four surface dimers (2x4 unit cell, obtained by doubling the 2x2 unit cell along the direction orthogonal to the dimer rows, n = 2). The adsorption energies of 23.0 (1.0 eV) , 37.4 (1.62 eV) , and 37.7 kcal/mol (1.63 eV) have been obtained, respectively. They have all been referred to the 2x2 reconstructed surface total energy. As already found for cyclopentene on the silicon (100) surface[50], the 1 ML coverage shows a smaller absorption energy due to the repulsive interaction of H atoms belonging to neighbour ACP molecules. The adsorption energy shows a monotonic increase with the coverage, almost reaching convergence for 0.5 ML. The converged value of about 37 kcal/mol (1.6 eV) shows a fair agreement with the 40 kcal/mol (1.7 eV) calculated in the cluster model, so that the two methods support each other satisfactorily.

	Si(1)-Si(2)		Si(2)-Si(3)		Si(3)-Si(2)-Si(4)		Buckling angle	
Model	PW	GTO	PW	GTO	PW	GTO	PW	GTO
$ACP-Si_9H_{12}$	2.352	2.326	2.352	2.347	111.2	108.7	0.0	0.0
$ACP-Si_{29}H_{32}$	2.347	2.327	2.358	2.350	110.5	110.1	0.0	0.0
ACP surface[a]	2.372		2.365		110.0		0.0	
ACP surface[b]	2.369		2.353		107.8		0.0	
	Si(1)-C(1)		Si(2)-C(2)		C(1)-C(2)		Si(1)-C(1)-C(2)	
Model	PW	GTO	PW	GTO	PW	GTO	PW	GTO
$ACP-Si_9H_{12}$	1.955	1.946	1.958	1.946	1.590	1.588	101.2	100.9
$ACP-Si_{29}H_{32}$	1.959	1.948	1.963	1.948	1.588	1.586	101.2	101.0
ACP surface[a]	1.975		1.974		1.568		101.8	
ACP surface[b]	1.963		1.951		1.576		102.4	

[a] 1-ML coverage.
[b] 0.5-ML coverage.

Table 2.12: Main geometrical parameter of the ACP adsorbtion on silicon clusters, shown in Fig 2.6 and 2.7, and on infinite surfaces optimized with GTOs and PWs basis functions.

	Potential energy differencies (kcal/mol)				With thermal corrections at 298 K (kcal/mol)			
	ΔE_{compl}	ΔE_{TS}	$\Delta E^{\ddagger}$	ΔE_{prod}	ΔG_{compl}	ΔG_{TS}	$\Delta G^{\ddagger}$	ΔG_{prod}
CEP-31G	-8.09	-1.53	6.55	-45.69	2.27	8.95	6.67	-34.05
CEP/6-31G(d,p)	-11.37	-5.03	6.34	-48.11	-1.01	5.45	6.46	-36.47
CEP/6-31+G(d,p)	-10.41	-4.36	6.05	-48.51	-0.05	6.12	6.17	-36.86
CEP/6-311+G(d,p)	-12.12	-5.83	6.29	-49.70	-1.76	4.65	6.41	-38.06
LANL2DZ	-4.59	0.20	4.79	-47.89	5.77	10.68	4.91	-36.25
LAN/6-31G(d,p)	-12.81	-7.14	5.67	-50.60	-2.45	3.34	4.79	-38.96
LAN/6-31+G(d,p)	-12.10	-6.67	5.42	-51.25	-1.74	3.81	5.54	-39.61
LAN/6-311+G(d,p)	-13.63	-7.97	5.65	-52.53	-3.27	2.51	5.77	-40.89
LAN+(d)/6-311+G(d,p)	-11.71	-5.49	6.22	-48.04	-1.35	4.99	6.34	-36.40

Table 2.13: Electronic (ΔE) and free (ΔG) energy differencies computed at PBE0 level with different basis sets and pseudopotentials for the cycloaddition reaction of ACP to the Si_9H_{12} cluster. Counterpoise correction are included in all calculations.

	Potential energy differencies (kcal/mol)				With thermal corrections at 298 K (kcal/mol)			
	ΔE_{compl}	ΔE_{TS}	$\Delta E^{\ddagger}$	ΔE_{prod}	ΔG_{compl}	ΔG_{TS}	$\Delta G^{\ddagger}$	ΔG_{prod}
CEP-31G	-10.13	-5.09	5.04	-46.01	0.56	6.32	5.76	-35.60
CEP/6-31G(d,p)	-12.86	-7.77	5.09	-48.86	-2.17	3.64	5.81	-38.45
CEP/6-31+G(d,p)	-11.12	-5.99	5.13	-49.78	-0.43	5.42	5.85	-39.37
CEP/6-311+G(d,p)	-12.75	-7.49	5.26	-51.11	-2.06	3.92	5.98	-40.70
LANL2DZ	-7.76	-4.07	3.68	-49.89	2.93	7.34	4.40	-39.48
LAN/6-31G(d,p)	-15.26	-10.42	4.84	-51.45	-4.57	0.99	5.56	-41.04
LAN/6-31+G(d,p)	-13.49	-8.60	4.88	-52.70	-2.80	2.81	5.60	-42.29
LAN/6-311+G(d,p)	-14.98	-10.00	4.98	-54.01	-4.29	1.41	5.70	-43.60
LAN+(d)/6-311+G(d,p)	-14.05	-8.78	5.27	-50.25	-3.36	2.63	5.99	-39.84

Table 2.14: Electronic (ΔE) and free (ΔG) energy differencies computed at PBE0 level with different basis sets and pseudopotentials for the cycloaddition reaction of ACP to the $Si_{29}H_{32}$ cluster. Counterpoise correction are included in all calculations.

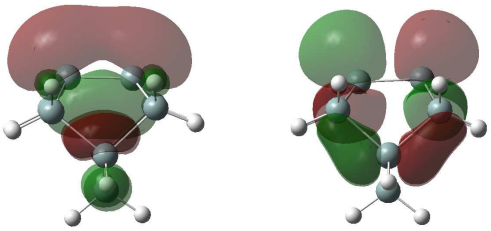

(a) HOMO orbital. (b) LUMO orbital.

Figure 2.10: HOMO and LUMO graphical representation of Si_9H_{12} cluster.

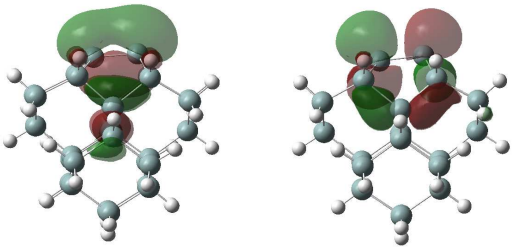

(a) HOMO orbital. (b) LUMO orbital.

Figure 2.11: HOMO and LUMO graphical representation of $Si_{29}H_{32}$ cluster.

2.3.3 Further Functionalization of Si Surface

In reference [31] it is reported that after the ACP reaction on Si(100)-2×1 surface further functionalization was performed attaching the sulfo-succinimidyl-4-(N-maleimidomethyl)-cyclohexane-1-carboxilate (SSMCC) bifunctional linker followed by another reaction so as to attach a modified thio-oligonucleotide. In such a way the silicon surface became sensitive to the complementary oligonucleotide demostrating the ability to detect single-base mismaches. In the following we refer on a conformational study, carried out at the PBE0/CEP-31G level, on a model system to describe such further functionalization on our clusters.

The model system to represent the thio-oligonucleotide chain has been chosen as just one uracil, while for the surface simulation it has been chosen the Si_9H_{12} cluster. These choices have been taken so as to simplify as much as possible the model sistem lightening the computational demands.

Geometry optimizations of the main conformational isomers have been done, computing also the vibrational correction at 1 atm and 298 K. We considered both chair (Fig. 2.12(a)) and boat (Fig 2.12(b)) isomers of cyclohexane in SSMCC. Furthermore, the axial isomer (Fig. 2.12(c)) and the isomer obtained rotating around the nitrogen amide bond axis (Fig. 2.12(d)) were also studied. In table 2.15 are reported the SCF and Gibbs Free energies expressed in kcal/mol of the isomers respect to the isomer in Fig. 2.12(a) while in fig-

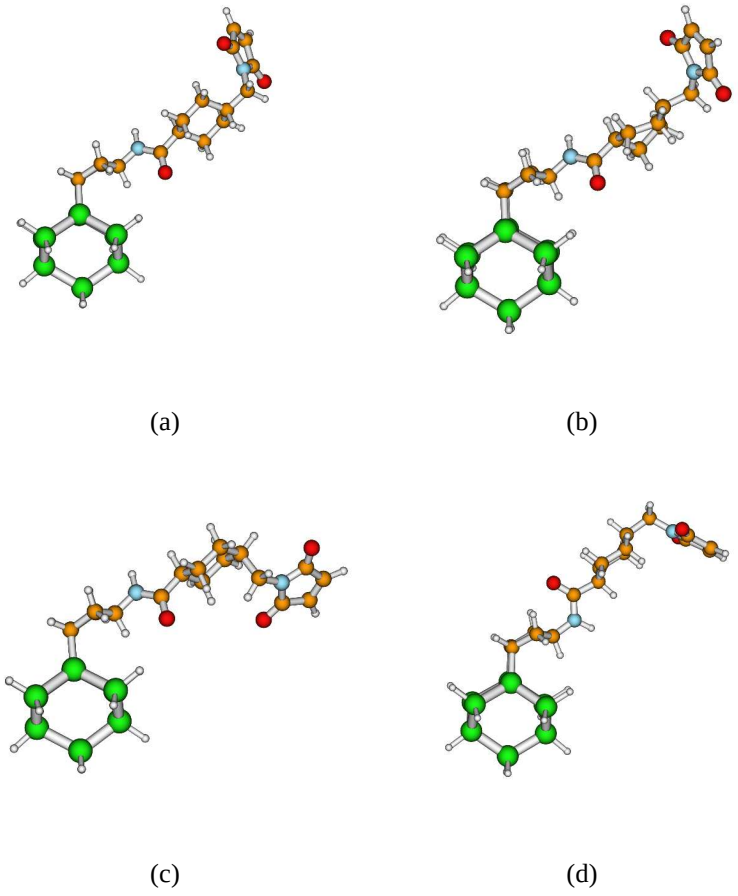

Figure 2.12: Conformational isomers of further functionalization product.

ures 2.13 and 2.14 are sketched the graphical representation of such data. Observing these data is evident, as expected, that the energies of the various isomers are very close to each other, so, a rapid interconversion among the different isomers is expected giving a rapidly interchanging dynamical scenario. However, considering better the isomer structure in Fig. 2.12 one has

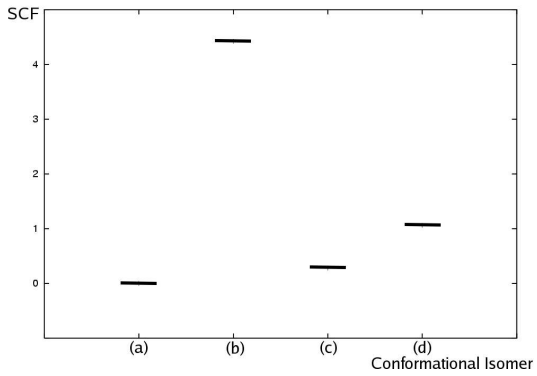

Figure 2.13: Graphical representation of SCF energies expressed in kcal/mol respect to isomer 2.12(a). See table 2.15 for the corresponding numerical values.

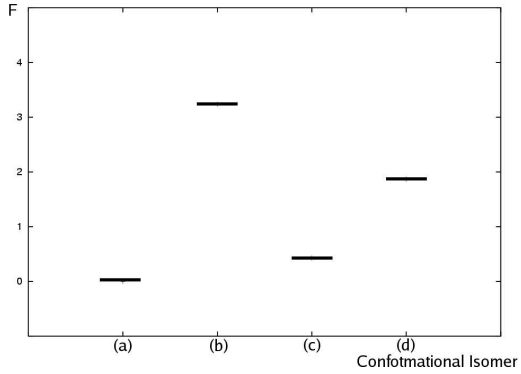

Figure 2.14: Graphical representation of Gibbs Free energies expressed in kcal/mol respect to isomer 2.12(a). See table 2.15 for the corresponding numerical values.

to conclude that such a surface model system can give only a qualitative description. Due to the length of the organic moiety it has to be expected that the

Isomer	SCF (kcal/mol)	F (kcal/mol)
(a)	0.0	0.0
(b)	4.4	3.2
(c)	0.3	0.4
(d)	1.1	1.9

Table 2.15: Corresponding numerical values of SCF energies in figure 2.13 and Gibbs Free energies of figure 2.14.

Si_9H_{12} cluster can not describe properly the interaction on the surface. Infact, expecially considering the isomer in Fig. 2.12(c), it is evident the shortness of surface model, so it is clear that for a better description of the isomers it is requiered a more extended surface. The same reasoning apply exactly in the same way for the $Si_{29}H_{32}$ cluster. In order to achieve a better description of such properties it is required a more extended surface model system.

2.4 Conclusions

In the present work we reported the full characterization of ACP reaction path along both chemical functionality outlying the effective competitiveness of both reactions on silicon surface reaction sites, justifying the use of protecting group chemistry. Differently from others works mainly focused on a radicalic mechanism, here we found another mechanism of reaction based on the separation of charges in silicon surface dimer with no radicals formation. For both ACP functionalities the raction occur by the formation of an intermediate complex followed by the formation of the final product through a transition state. The complex formation seems to increase the reactivity of surface increasing the nucleophilic character of silicon atom involved in the next step of reaction.

The main results of the comparative study of ACP adsorption and reaction on the (100) silicon surface by DFT methods based both on localized GTO and delocalized PW basis functions have also been presented. The silicon surface has been modeled by clusters of increasing dimension and by periodic slabs. The modelling of reconstructed surface with both methodologies were consistent with each other and all reproduce the main physical chemical properties of such a system. With all methods investigated a buckling of the silicon dimer on surface was found, consistently with experimental observations. The PBE0 model, the only one for which there are some attempt to balance dynamical

and statical electron correlations due to the introduction of exact Hartree-Fock exchange energy not allowed within PW's formalism is likely to provide the most reliable structural results.

The results obtained with Gaussian type orbitals (GTO) and plane wave (PW) basis functions with the same density functional are in fair agreement, provided a fine tuning of both basis sets is done to ensure full convergence.

The results obtained for the cluster model are in good agreement with those issuing from slab calculations on infinite silicon surfaces , concerning both the structural properties and the product energies.

On these grounds it is possible to consider the methodology based on GTO computations with the hybrid functional PBE0, extended basis set, and correction of BSSE as a valid computational protocol that can provide quite reliable estimates of kinetic and thermodynamic parameters. For the reaction studied here it has been found the values are -40 and 6 kcal/mol for reaction and activation free energies, respectively. This results seem to be in agreement with experimental observations.

Furthermore, it has been considered a further step in the surface functionalization considering the product of reactions of SSMCC and thio-oligonucleotide on the ACP hybrid surface. In this case, it has been put in evidence the inadequacy of such a surface model system due to its shortness, requiring larger model system.

Conclusions

In the present work we have considered various topics concerning spectroscopic properties simulation (Part I) and basic aspects involved in nanoscience (Part II).

In the first part the IR spectra of uracil in vacuo was simulated. The simulated IR spectrum was obtained by the Fourier Transform of the dipole autocorrelation function. This function has been generated by the sampling of the 10ps ADMP (*ab initio* Density Matrix Propagation) trajectory.

The results were compared with the experimental spectra of uracil in argon matrix so as to reproduce as much as possible the neglect of intermolecular interaction characteristic of the current simulation conditions. Moreover, the results were also compared with frequencies calculations within harmonic and anharmonic approximations. The simulated spectrum present a satisfactory agreement with experimental data with a mean error of 125 cm^{-1} and reproducing the main features of the spectra. With respect to computed data the simulated results have given intermediate performances. That is, present method represents an improvement with respect to harmonic frequencies calculation but not for anharmonic frequencies that remain a better description anyway. The mean error found were 33 and 17 cm^{-1}, respectively.

Further improvements toward the biological chemical environments could be achieved by the introduction of solvent effect, that could be done with the explicit inclusion of solvent molecules or within the PCM model or even both.

In the second part, we studied basic aspects related to the synthesis of DNA/RNA biosensors. The study were centered mainly on the addition reaction of 1-amino-3-cyclopentene (ACP) on the surface, that constitutes the first step to obtain an hybrid surface. Infact, after this reaction the surface presents a free amino group suitable for further functionalizations. This reaction has been studied in collaboration with the Departement of Physics of the University of Naples "Federico II" in order to compare computational results obtained with different methodologies. In particular, we compared results obtained within density functional theory (DFT) with both Gaussian Type Orbitals and Plane Waves basis set functions.

To simulate the Si(100)-2×1 surface we used both clusters (Si_9H_{12} and $Si_{29}H_{32}$) and slabs models.

The modelling of reconstructed surface with both methodologies were consistent to each other and all reproduces the main physical chemical properties of such a system. With all methods investigated a buckling of the silicon dimer on surface was found, consistently with experimental observations.

Full characterization of ACP reaction path along both chemical functionalities was reported outlying the effective competitiveness of both reactions on silicon surface reaction sites, justifying the use of protecting group chemistry.

The results obtained with Gaussian type orbitals (GTO) and plane wave (PW) basis functions with the same density functional are in fair agreement, provided a fine tuning of both basis sets is done to ensure full convergence.

The results obtained for the cluster model are in good agreement with those issuing from slab calculations on infinite silicon surfaces , concerning both the structural properties and the product energies.

On these grounds it is possible to consider the methodology based on GTO computations with the hybrid functional PBE0, extended basis set, and correction of BSSE as a valid computational protocol that can provide quite reliable estimates of kinetic and thermodynamic parameters. For the reaction studied here the values -40 and 6 kcal/mol are found for reaction and activation free energies, respectively. These results seem to be in agreement with experimental observations.

Furthermore, it has been considered a further step in the surface functionalization considering the product of reactions of SSMCC and thio-oligonucleotide on the ACP hybrid surface. In this case, it has been put in evidence the inadequacy of such a surface model system due to its shortness, requiring more extended model system.

List of Figures

List of Tables

Bibliography

[1] D.Frenkel and B.Smit. *Understanding Molecular Simulation*. Academic Press, San Diego, CA, **1996**.

[2] R.Ahlrichs S.Elliot and U.Huniar. *Modern methods and algorhitms of quantum chemistry*, volume 3, chapter *Ab initio* treatment of large molecules. Julic, Germany, **2000**.

[3] A.Szabo and N.S.Ostlund. *Modern Quantum Chemistry*. Dover Publications, **1996**.

[4] A.Schäfer. *Modern methods and algorhitms of quantum chemistry*, volume 1, chapter Industrial challenge for quantum chemistry. Julic, Germany, **2000**.

[5] R.G.Parr and W.Yang. *Density Functional Theory of Atoms and Molecules*. Oxford University Press, **1989**.

[6] H.B. Schlegel J.M. Millam S.S. Iyengar G.A. Voth A.D. Daniels G.E. Scuseria and M.J. Frisch. *J.Chem.Phys.*, 114(22):9758, **2001**.

[7] R.M.Silverstein G.C.Bassler and T.C.Morril. *Spectrometric Identification of Organic Compounds*. John Wiley and Sons, New York, **1963**.

[8] D.Marx and J.Hutter. *Modern methods and algorhitms of quantum chemistry*, volume 1, chapter *Ab initio* molecular dynamics: theory and implementation. Julic, Germany, **2000**.

[9] R.Car and M.Parrinello. *Phys.Rev.Lett.*, 55(22):2471, **1985**.

[10] H.Goldstein. *Classical Mechanics*. Addison-Wesley, Cambridge, **1980**.

[11] D.A.McQuarrie. *Statistical Mechanics*. University Science Book, California, **2000**.

[12] M.P.Gaigeot and M.Sprik. *J.Phys.Chem. B*, 107:10344, **2003**.

[13] W.H.Press S.A.Teukolsky W.T.Vetterling and B.P.Flannery. *Numerical Recipes in C++, The Art of Scientific Computing*. Cambridge University Press, Cambridge, **2002**.

[14] M.J.Frisch G.W.Trucks H.B.Schlegel V.Barone M.Cossi G.Scalmani N.Rega *et al.* *GAUSSIAN 03 (Release C.02)*. Gaussian, Inc., Pittsburgh PA, **2003**.

[15] V.Barone. *In preparation*.

[16] V.Barone G.Festa A.Grandi N.Rega and N.Sanna. *Chem.Phys.Lett.*, 388:279, **2004**.

[17] A.D.Becke. *J.Chem.Phys*, 98:5648, **1993**.

[18] A.Les L.Adamowicz and M.J.Lapinski. *Spectrochim. Acta*, 48A:1385, **1992**.

[19] M.Nonella G.Mathias and P.Tavan. *J.Phys.Chem. A*, 107:8638, **2003**.

[20] M.Cossi N.Rega G.Scalmani and V.Barone. *J.Chem.Phys.*, 114:5691, **2001**.

[21] H.N.Waltenburg and J.T.Yates Jr. *Chem.Rev.*, 95:1589, **1995**.

[22] R.J.Hamers and Y.Wang. *Chem.Rev.*, 96:1261, **1996**.

[23] J.M.Buriak. *Chem.Rev.*, 102(5):1271, **2002**.

[24] W.Pan T.Zhu and W.Yang. *J.Chem.Phys.*, 107:3981, **1997**.

[25] R.Terborg P.Baumgartel R.Lindsay O.Schaff T.Giessel J.T.Hoeft M.Polcik R.L.Toomes S.Kulkarmi A.M.Bradshaw and D.P.Woodruff. *Phys.Rev. B*, 61:16697, **2000**.

[26] J.H.Cho L.Kleinman C.T.Chan and K.S.Kim. *Phys.Rev. B*, 63:3306, **2001**.

[27] S.F.Bent. *J.Phys.Chem. B*, 106:2830, **2002**.

[28] W.Göpel. *Biosensors and Bioelectronics*, 13:723, **1998**.

[29] T.Vo-Dinh J.P.Alarie N.Isola D.Landis A.L.Wintenberg and M.N. Ericson. *Anal.Chem,* 71:358, **1999**.

[30] T.Knickerbocker T.Strother M.P.Schwartz J.N.Russel Jr J.Butler L.M.Smith and R.J.Hamers. *Lang.*, 19:1938, **2003**.

[31] Z.Lin T.Strother W.Cai X.Cao L.M.Smith and R.J.Hamers. *Lang.*, 18:788, **2002**.

[32] T.Strother W.Cai X.Zhao R.J.Hamers and L.M.Smith. *J.Am.Chem.Soc.*, 122:1205, **2000**.

[33] M.Ono A.Kamoshida N.Matsuura E.Ishikawa T.Eguchi and Y.Hasegawa. *Phys.Rev. B*, 67:201306, **2003**.

[34] N.C.Handy and A.J.Cohen. *Mol.Phys.*, 99(5):403, **2001**.

[35] A.J.Cohen and N.C.Handy. *Mol.Phys.*, 99(7):607, **2001**.

[36] J.P.Perdew K.Burke and M.Ernzerhof. *Phys.Rev.Lett.*, 77:3865, **1996**.

[37] C.Adamo and V.Barone. *J.Chem.Phys.*, 110:6158, **1999**.

[38] T.R.Cundari and W.J.Stevens. *J.Chem.Phys.*, 98:5555, **1993**.

[39] P.J.Hay and W.R.Wadt. *J.Chem.Phys.*, 82:299, **1985**.

[40] G.Festa M.Cossi V.Barone G.Cantele D.Ninno and G.Iadonisi. *J.Chem.Phys.*, 122:184174, **2005**.

[41] N.W.Ashcroft and N.D.Mermin. *Solid State Physics*. Sounders College, Philadelphia, **2000**.

[42] J.Shoemaker L.W.Burggraf M.S.Gordon. *J.Chem.Phys.*, 112(6):2994, **2000**.

[43] O.Paz A.J.R.da Silva J.J.Saenz and E.Artacho. *Surf.Sci.*, 482-485:458, **2001**.

[44] S.H.Vosko L.Wilk and M.Nusair. *Can.J.Phys.*, 58:1200, **1980**.

[45] T.Ziegler. *Chem.Rev.*, 91:651, **1991**.

[46] S.F.Boys and F.Bernardi. *Mol.Phys.*, 19:553, **1970**.

[47] F.F.Murguet and G.W.Robinson. *J.Chem.Phys.*, 102(9):3648, **1995**.

[48] H.Preuss H.Stoll U.Wedig and TH.Krüger. *J.Int.Quant.Chem.*, 19:113, **1981**.

[49] M.Dolg. *Modern methods and algorhitms of quantum chemistry*, volume 1, chapter Effective Core Potentials. Julic, Germany, **2000**.

[50] J.H.Cho and L.Kleinman. *Phys.Rev. B*, 64:235420, **2001**.